Characterization and origin of low-T willemite (Zn2SiO4) mineralization: the case of the Bou Arhous deposit (High Atlas, Morocco)

Flavien Choulet, Luc Barbanson, Martine Buatier, Richard James, Torsten Vennemann, Aomar Ennaciri, Mohamed Zouhair

Characterization and origin of low-T willemite (Zn_2SiO_4) mineralization: the case of the Bou Arhous deposit (High Atlas, Morocco)

Choulet Flavien[1], Barbanson Luc[2], Buatier Martine[1], Richard James[1], Vennemann Torsten[3], Ennaciri Aomar[4], Zouhair Mohamed[4]

[1]: Chrono-Environnement, UMR6249, Université de Bourgogne Franche-Comté/CNRS, Besançon, France

[2]: Institut des Sciences de la Terre d'Orléans, UMR7327, Université d'Orléans/CNRS/BRGM, Orléans, France

[3]: Institut des Dynamiques de la Surface Terrestre, Université de Lausanne, Lausanne, Switzerland

[4]: Managem Group, Casablanca, Morocco

Willemite (Zn_2SiO_4) usually reported in hypogene non-sulfide deposits is described as the main ore mineral in the carbonate-hosted Bou Arhous zinc deposit. This deposit is located in the High Atlas intracontinental range that formed during the Tertiary. Based on a set of microscopic observations, it was possible to establish that willemite replaces primary sphalerite. On the basis of cathodoluminescence imaging, three successive generations of willemite are distinguished, with evidence of dissolution-reprecipitation processes. Willemite is also variably enriched in Ge (up to 1000 ppm), while Ge contents lower than 100 ppm are reported in the primary sulfide minerals. Depending on the willemite generation, this substitution was positively or negatively correlated to the Zn-Pb substitution. According to the nature of zoning (sector versus oscillatory), the incorporation of Ge was either controlled by

crystallographic factors or by the nature of the mineralizing fluids. Willemite is associated with other oxidation-related mineral species, like cerussite ($PbCO_3$), but is not in isotopic equilibrium and therefore not considered to be cogenetic. Oxygen isotope compositions support the formation of willemite at temperatures below 130 °C, from mixed meteoric and deeper, hydrothermal fluids. The formation of the High Atlas Belt during the Tertiary has contributed to the exhumation of the sulfide minerals and the development of vertical conduits for percolation of meteoric water and ascending hydrothermal fluids. In addition to a local contribution of silicate minerals of the host limestone, hydrothermal fluids probably transported Si and Ge that are incorporated in willemite.

Keywords: willemite, non-sulfide zinc ore deposit, cathodoluminescence, germanium, stable isotopes, Morocco

Introduction

Unconventional non-sulfide zinc deposits have been the focus of many studies during the last two decades (e.g. Boni and Mondillo 2015). In addition to an evaluation of their economic potential, efforts have been made to establish and update the classification of non-sulfide zinc ore deposits (e.g. Hitzman et al. 2003; Boni and Large 2003). Presently, it is accepted that several types of deposits are distinguished. The supergene deposits formed by weathering of primary sulfides at surface temperature (see a review in Boni and Mondillo 2015). The hypogene deposits include: i) primary hydrothermal high-temperature zinc silicate deposits (e.g. Vazante in Brazil, Monteiro et al. 2006; or Beltana in Australia, Groves et al. 2003); ii)

51 secondary metamorphosed deposits (e.g. Franklin and Sterling Hill in USA; Johnson
52 et al. 1990) and iii) secondary low-temperature (<100 °C) Zn carbonate deposits (e.g.
53 Angouran in Iran, Boni et al. 2007; Daliran et al. 2013).

54 The occurrence of willemite (Zn_2SiO_4) is generally considered to be testimony
55 of a formation at relatively hot conditions (between 200 and 300 °C) under oxidizing
56 and alkaline conditions (Brugger et al. 2003). However, the origin of willemite is
57 controversial (Pough 1941), as the geological features of numerous willemite-rich
58 deposits are considered to derive from low-temperature (< 100 °C) hydrothermal
59 processes or supergene weathering. The historical deposits of Belgium in the Namur-
60 Verviers Synclinorium district include carbonate-hosted willemite ores whose origin
61 remains disputed (Dejonghe 1998; Boni et al. 2005; Coppola et al. 2008). Based on
62 ore characteristics and fluid inclusions, Coppola et al. (2008) hypothesized that
63 willemite may result from low-temperature hydrothermal processes caused by
64 oxidizing fluids with high silica activities. In addition to hypogene/hydrothermal
65 willemite (Boni et al. 2011), supergene willemite directly replacing primary sphalerite
66 has been described in the Namibian and Zambian carbonate-hosted oxidized zinc
67 deposits. The crystal habits, together with the mineral association and the presence of
68 monophase fluid inclusions, support a meteoric origin of the mineralizing fluids or at
69 least low-temperature hydrothermalism (Terracciano 2008). However, the presence of
70 supergene willemite in such carbonate-hosted environments is clearly a paradox.
71 Smithsonite ($ZnCO_3$) or hydrozincite ($Zn_5(CO_3)_2(OH)_6$) are supposed to be stable in
72 the weathering zone (Reichert and Borg 2008). At 25 °C, willemite may precipitate
73 instead of smithsonite at low CO_2 fugacity (log f_{CO2}<-1.6) and in the presence of silica
74 (log a_{quartz}>-3) (Brugger et al. 2003). However, this model does not consider the
75 possibility to precipitate hemimorphite. According to McPhail et al. (2003; 2006),

hemimorphite is stable with respect to willemite at temperatures below 90-100 °C. This may explain why hemimorphite ($Zn_4Si_2O_7(OH)_2 \bullet (H_2O)$) is frequently reported in supergene deposits (Hitzman et al. 2003). Hence, the presence of willemite is frequently explained by the direct precipitation from low-temperature hydrothermal fluids (Coppola et al. 2008; Terracciano 2008).

Zinc silicate is a versatile luminescent mineral that has been widely used as a phosphorescent agent in displays and lighting devices (Takesue et al. 2009). Based on studies of natural Mn-rich samples from Franklin or Sterling Hill deposits, USA (Palache 1935), it has been shown that Mn^{2+} guest ions are natural luminescence activators in willemite, which emits in a green color (Bhalha and White 1972). Green willemite has been reported from hypogene deposits (Monteiro et al. 2007; Boni et al. 2011), while willemite from presumed supergene or low-temperature ores luminesces in dull to bright blue (Coppola et al. 2008; Terracciano 2008; Melcher et al. 2009). Although the origin of the blue emission is not clearly established and probably due to activator or quenching ions other than Mn^{2+}, cathodoluminescence (CL) imaging enables to reveal the different mineralization stages and may be used as a tool to discriminate the origin of willemite.

The Bou Arhous deposit in Morocco exposes a non-sulfide ore that contributed to the infilling of a large karst developed in Jurassic limestone (Leblanc 1968). The mined ore mainly consists of willemite associated with supergene or karst-related minerals (Choulet et al. 2014, 2015). Except for the primary sulfide mineralization, no evidence of a later hydrothermal event or Si-rich fluid input has been reported yet. In this study, we present a detailed investigation of the willemite ore texture coupled with a determination of its major and trace element composition.

In addition, stable isotope composition of willemite and cerussite are used to constrain the characteristics of the mineralizing fluids and discuss the origin of willemite ores.

The Bou Arhous deposit

The Bou Arhous deposit is located in the High Atlas range, in the Central-Eastern part of Morocco (Fig. 1a). The High Atlas range results from Tertiary intracontinental deformation related to the closure of the Tethys (Frizon de la Motte et al. 2000). The range consists of a fold-and-thrust belt with narrow anticlinal ridges and large synclinal plains. Folded units are mainly composed of Jurassic limestone and marl sequences that were originally emplaced into a horst and graben system related to the opening of the Tethyan and Atlantic oceans (Laville and Piqué 1991). Tertiary thrusts, rooted in the Triassic shales, reactivated the Jurassic normal faults. These faults delimitated the horst and graben domains, characterized by contrasted sedimentary infilling.

The Moroccan High Atlas range hosts hundreds of base metal deposits and occurrences that belong to the circum-Mediterranean Zn-Pb province (Rouvier et al. 1995). Several periods of ore deposition were distinguished (Mouguina 2004; Choulet et al. 2014; Charles et al. 2016): 1) the Lower Jurassic with the emplacement of stratabound Zn-Pb-Fe sulfides, 2) the Middle Jurassic including Cu-Ni and Zn-Pb mineralization genetically associated with mafic magmatism, and 3) the Tertiary, characterized by the supergene evolution of the aforementioned Jurassic deposits. For this latter case, the supergene enrichment was strongly controlled by tectonics, which enabled the exhumation of deep sulfide lenses and the development of faults that served as drains for descending meteoric waters (Choulet et al. 2014).

Hosted in one of the High Atlas anticlinal ridges (Fig. 1b), the Bou Arhous ore deposit is enclosed in Lower Sinemurian massive limestone ($l_{1\text{-}2}m$), to the south of the Grand Accident Fault, a syn-sedimentary normal fault that was inverted during the Tertiary (Leblanc 1968). At the mine, the bedding is steep to vertical and even overturned (Fig. 2a). The limestone has developed a 120-m thick karst that extends over 18,000 m^2 (Fig. 1b); sinkholes and tunnels are filled with detrital and residual clays (Buatier et al. 2016; Choulet et al. 2016). The mineralization consists of a network of interconnected vertical veins that meet the karst cavities (Fig. 2b). The width of the veins may reach up to 10 meters. A vertical zonation of the mineralogical associations is given with preserved sulfide minerals (sphalerite and galena) at depth and newly formed non-sulfide minerals towards the surface (Choulet et al. 2014).

The Bou Arhous deposit is currently mined by Managem and reserves have been estimated at 250 kt, grading 16 % Zn and 4 % Pb. The non-sulfide ore is mainly composed of willemite and minor smithsonite, hydrozincite and hemimorphite. Remnant galena and cerussite are associated with willemite forming black aggregates (Fig. 2c). This black ore is often embedded in various clayey materials (Fig. 2d). The barren red clays are of residual and detrital origin, linked with the development of the karst system, whereas the white to ochre zinc clays are newly formed after willemite dissolution (Choulet et al. 2016). Ore is processed at the site of Guemassa, south of Marrakech since 2002, using hydrometallurgy to produce a ZnO concentrate as the final product. Leaching by H_2SO_4 allows zinc recovery from oxidized ores, whatever the mineralogy of the raw material (zinc silicates, carbonates or hydrated phases, but not sulfide minerals).

Material and methods

150

151 Sample preparation and microscopic observation

152

153 Hand samples of black ore were collected in the different mine levels and cut
154 to prepare a set of 30 polished thin-sections. Whole-rock powders were also used for
155 X-ray diffraction (XRD) measurements. Procedure and results may be found in
156 Choulet et al. (2016). A first optical investigation using a Leica DMRX petrographic
157 microscope was complemented by Scanning Electron Microscopy (SEM) at the
158 FEMTO-ST Institute (Université de Bourgogne Franche-Comté, France). Back-
159 scattered electron (BSE) imaging operated at 15 kV in low vacuum conditions was
160 combined with semi-quantitative analysis using Energy-Dispersive Spectrometers
161 (EDS). Cold cathodoluminescence (CL) observations using OPEA instrumentation
162 hosted at Chrono-Environnement (Université de Bourgogne Franche-Comté) were
163 made with an acceleration voltage of 18.5 ± 1.5 keV and a current of 350 ± 150 mA to
164 investigate zoning in willemite and establish relationships with other minerals.
165 Additional spectral analyses were performed with a Zeiss MCS CCD UV-NIR
166 spectrophotometer.

167

168 Micro-analyses

169

170 The major element composition of sphalerite, galena and willemite was
171 obtained by Electron Probe Micro-Analysis (EPMA), at University of Lausanne,
172 Switzerland, using a JEOL 8200 Superprobe equipped with five Wavelength
173 Dispersion Spectrometers (WDS). Carbon-coated polished thin-sections were
174 analyzed with a beam of 20 kV for sulfide minerals and 15 kV for willemite,

175 respectively, and a current of 10 nA. The resolution is ca. 1 μm. Oxides, silicates and
176 pure metals were used as standards. Only analyses between 97 and 103 wt% were
177 retained for discussion.

178 Complementary LA-ICP-MS measurements of the Ge content were made on a
179 quadripolar Agilent 7500 ICPMS coupled with a 193 nm excimer Resonetics M-50E
180 laser hosted at the Université Blaise-Pascal, Clermont-Ferrand, France. The laser was
181 set up to produce an energy density of ca. 4 $J.cm^{-2}$ at a repetition rate of 2 Hz. The
182 laser spot size was 20 μm in diameter. The following isotopes were monitored: ^{29}Si,
183 ^{66}Zn, ^{67}Zn, ^{68}Zn, ^{70}Ge, ^{72}Ge, ^{73}Ge, ^{74}Ge and ^{76}Ge. The total acquisition time
184 (background and signal) was limited to 100 s for one spot. Data reduction was carried
185 out with Glitter software. Zinc content previously measured by EPMA was used as an
186 internal standard. By comparing the recalculated Si and the EPMA-measured Si, it
187 appears that ^{67}Zn is the most suitable isotope for calibration. NIST 610 and NIST 612
188 were used as external standards (Pearce et al., 1997). While ^{70}Ge and ^{76}Ge were not
189 considered due to interference with ^{70}Zn and Ar isotopes, no significant differences
190 were observed between the three other Ge isotopes. ^{72}Ge was probably
191 underestimated because of a possible interference with $^{56}Fe^{16}O$. As the abundance of
192 ^{74}Ge (36.28%) largely exceeds that of ^{73}Ge (7.73%), ^{74}Ge was retained for the
193 quantification of Ge in willemite.
194
195 Stable isotope analyses
196
197 Stable isotope analyses of ore and host limestone were done at the University
198 of Lausanne. 11 willemite and 7 carbonate (cerussite, calcite and dolomite)
199 concentrates were separated from the 200 μm milled fraction by heavy liquid methods

200 using LST Fastfloat ® liquor and filters. Grains were further handpicked under a
201 binocular microscope. The purity of concentrates was checked by XRD and only
202 reflections corresponding to cerussite or willemite were observed in the respective
203 samples. Because of the small size of the crystals, it was not possible to separate the
204 different generations of willemite and cerussite and only bulk compositions are
205 provided.

206 O_2 was extracted from willemite by using a CO_2-laser line linked to a Finnigan
207 MAT 253 spectrometer. Between 1.5 to 2.5 mg of sample was loaded onto a small Pt-
208 sample holder and pumped out to a vacuum of about 10^{-6} mbar. After pre-fluorination
209 of the sample chamber, the samples were heated with a CO_2-laser in the presence of
210 50 mbar of pure F_2. Excess F_2 was separated from the O_2 produced by conversion to
211 Cl_2 using KCl held at 150 °C. The extracted O_2 was then introduced into the inlet of a
212 mass spectrometer. The detailed procedure may be found in Kasemann et al. (2001).
213 Oxygen isotope compositions are given in the standard δ-notation, expressed relative
214 to the Vienna Standard Mean Ocean Water (VSMOW) in permil (‰). Replicate
215 oxygen isotope analyses of the LS-1 in-house quartz standard had an average
216 precision of ± 0.03 ‰ (n = 5) for $\delta^{18}O$ and all values are normalized to a value of 9.64
217 ‰ for NBS-28 quartz with an average accuracy better than 0.2 ‰.

218 The C and O isotopic composition of carbonates was determined using a
219 GasBench II automated system interfaced to a Thermo Finnigan Delta PlusXL mass
220 spectrometer. The procedure is adapted after Spötl and Vennemann (2003). Oxygen
221 isotope analyses were corrected using the phosphoric acid fractionation at 70°C for
222 calcite (1.10087; Swart et al. 1991), for dolomite (1.0099; Rosenbaum and Sheppard
223 1986) and cerussite (1.00911; Gilg et al. 2003). The data are reported in the
224 conventional δ-values as ‰ deviations relative to the Vienna Pee Dee Belemnite

225 (VPDB) standards for C isotopes and to the VSMOW for O isotopes. Replicate
226 isotope analyses of the in-house standard used (CM) had an average precision of ±
227 0.04 ‰ for $\delta^{13}C$ and ± 0.07 ‰ for $\delta^{18}O$ (n = 4).
228
229 **Results**
230
231 Host rock and ore characterization
232
233 The host rock of the Bou Arhous mineralization is a massive fine-grained grey
234 to bluish-grey limestone. This micritic limestone locally includes coarse fragments of
235 echinoderms and lamellibranchs (Leblanc 1968). Idiomorphic quartz crystals are
236 frequently found in the micritic limestone as well as secondary sparite (Fig. 3a).
237 Despite a general euhedral shape, quartz grains often display a skeleton-like aspect,
238 suggesting dissolution (Fig. 3a), with evidence of late sparite precipitated in the newly
239 formed porosity. In addition, the bulk composition of the massive limestone has high
240 MgO contents (up to 13 wt%) that can be explained by a pervasive dolomitization
241 also revealed by XRD patterns (Choulet et al. 2016). Cathodoluminescence imaging
242 shows large dolomite crystals luminescing red within the micrite (Fig. 3b). In some
243 cases, dolomite may be altered and replaced by calcite. Small cavities or sinkholes are
244 filled with sparite with yellow luminescence (Fig. 3c). At the edge of the cavity, an
245 accumulation of dolomite rhombs and idiomorphic quartz is observed (Fig. 3c). This
246 stack of insoluble minerals differs from their random distribution in the preserved
247 micritic facies.
248 According to the XRD results, the ore is composed of willemite, cerussite,
249 galena and clays, associated with calcite, quartz and dolomite from the gangue and the

host rocks (Choulet et al. 2014; 2016). Remnant sulfide minerals include sphalerite and galena. In thin-sections, corroded sphalerite can be seen as embedded in willemite (Figs. 4a and 4g) and secondary galena (Gn II) has precipitated onto the rim of partly dissolved sphalerite or along fractures cutting euhedral sphalerite (Figs. 4b and 4h). Like the host micrite, willemite includes idiomorphic quartz crystals, exposing fractures and evidence of corrosion (Fig. 4b). An irregular rim of anglesite locally coats the galena (Gn I) and is itself transformed into cerussite (Fig. 4c). Frequently, only granular cerussite that armors galena is observed and this assemblage often constitutes the core of the euhedral willemite crystals (Figs. 4d and 4e). This latter type of cerussite (Cer I) must not be mistaken for the late tabular crystals of cerussite (Cer III) observed in the druses (Fig. 4e). Clusters of thin tabular crystals of barite are found in association with willemite and cerussite (Figs. 4f to 4h) or as late overgrowths within the geodes. Two types of willemite crystals have been found in all thin-sections. While small barrel-shaped crystals are found in the equigranular ore facies (Fig. 4d), radial-fibrous aggregates locally form a botryoidal facies (Fig. 5a). In both cases, willemite crystals may display an irregular outline suggesting dissolution, with zinc clays growing over willemite and filling the newly formed porosity (Fig. 5b). These clay minerals associated with detrital quartz (Fig. 5c) correspond to the white clayey material that encompasses the willemite ore (Fig. 2d); they were described in detail by Buatier et al. (2016) and Choulet et al. (2016). Radial-fibrous willemite aggregates seem to postdate early cerussite (Cer I, often associated with Gn I) and predate late cerussite infilling (Cer III, without galena) (Figs. 5d and 5e). In addition, cerussite (Cer II) bands are intercalated between the different stages of willemite growth (Fig. 5f).

As outlined above, several morphotypes of willemite may be found. This includes: 1) idiomorphic barrel-shaped crystals (Fig. 6a), which are frequently twinned (Fig. 6b) and 2) radial-fibrous aggregates or spherulites (Figs. 6c and 6d). These crystal types must not be confused with the successive generations of willemite that are described in the following section.

Identification of willemite generations

CL imaging was used for deciphering the successive generations of willemite. The Bou Arhous willemite luminesces in blue from dull indigo to bright greenish-blue. Three successive generations were distinguished:

- Willemite Ia (Wil Ia), which partly refers to the prismatic morphotype (Fig. 6a) is characterized by sectoral zoning with sectors identified by their luminescence (Fig. 7a). Deep indigo sectors seem to be associated with particular faces, whilst bright blue sectors correspond to other faces. When crystals display penetration twinning, pseudo-patchy zoning with an irregular dark and bright chessboard pattern is observed. The extreme stage of multiple twinning corresponds to the second morphotype of willemite, spherulites (Figs. 6c and 6d), which exhibit a radial distribution of triangular dark sectors separated by thin bright sectors (Fig. 7b).
- Willemite Ib (Wil Ib) exhibits well-defined oscillatory zoning characterized by a fine alternation of bright blue and dark indigo bands (Fig. 7b). Wil Ib always develops on a core crystal, usually Wil Ia, with a sharp transition from sectoral to oscillatory zoning (Figs. 7a and 7b). Individual willemite spherulites may be merged to form aggregates, rimmed by banded willemite (Fig. 7c).

- Willemite II (Wil II) corresponds to small grains that precipitate in the pores between the aggregates of banded willemite or the willemite spherulites (Fig. 7d). They systematically form after a major dissolution stage affecting both Wil Ia and Wil Ib, as evidenced by the convolute or truncated shape of crystals (Figs. 7e and 7f). This dissolution stage is accompanied by the pervasive development of thin interconnected fractures filled with cerussite (Figs. 7c and 7f) that luminesces in bright bluish white.

Composition of sulfide minerals and willemite

The mineral compositions of sulfides (galena and sphalerite) were obtained by Electron Microprobe Analyzer (EPMA) and are given in Table 1. Sphalerite is poor in Fe (<0.1 wt%) and minor elements were not detected. For galena, the minor element content is low except for Ag, which may reach up to 0.3 wt%.

The composition of the different generations of willemite was obtained by EPMA and LA-ICPMS methods and results are reported in Table 2. The total oxide content averages 99 wt%, with a standard deviation between 0.3 and 0.6 wt%. The major oxide content (ZnO and SiO_2) slightly varies (1 to 2 wt%) between the different generations of willemite (Table 2). Willemite does not contain major impurities, except for PbO that may reach up to 2 wt% (Table 2). No Mn was detected in the different generations of willemite. The Ge content analyzed by LA-ICPMS was compared to the Ge content recalculated from EPMA-measured GeO_2. Despite slight differences, both datasets have the same trend and a similar range of element contents. Significant differences between willemite sectors distinguished by CL imaging may be noticed. While the dark sectors of Wil Ia have a low Ge content (less than 200

ppm) and a high PbO content (up to 2 wt%), the light sectors have significant Ge contents with up to 1100 ppm (Figs. 8a and 8b). In both cases, the relative standard deviation is low (Table 2). In contrast, the values for Ge in Wil Ib are irregularly distributed with a range from 22 to 858 ppm and high standard deviation (Table 2). Ablation spots were too large, compared to the growth bands of oscillatory-zoned crystals (Fig. 8b). But, using EPMA, it was possible to analyze each band, and no direct connection between the Ge content and the luminescence of the Wil-Ib crystals are observed. The range for PbO content is between 0.06 and 0.84 wt% (Table 2). For Wil II, the Ge content is below the detection limit and the PbO content ranges are similar to those of other willemite generations.

In the individual Wil Ia crystals, a correlation between the Ge and Si contents is marked by an extremely well-constrained trend line with a negative slope (Figs. 8c and 8d). Despite an apparent random distribution, a similar trend is observed for all data from Wil Ia and Wil Ib crystals (Fig. 8e). The Ge enrichment in willemite is accompanied by a lower concentration of Si. When comparing the Zn and Pb contents, differences between the different types of willemite are noted. While there is no apparent correlation between Zn and Pb for Wil Ib, a well-defined trend with a negative slope is observed for Wil Ia and Wil II (Fig. 8f).

Stable isotope compositions

Results of the stable isotope analyses on bulk willemite, bulk cerussite and host carbonate samples are given in Table 3. For willemite, $\delta^{18}O$ values range from 5.3 to 7.8 ‰, except for sample BA136 ($\delta^{18}O$ = 15.6 ‰) that was contaminated by the in-house quartz standard during laser extraction. While the $\delta^{18}O$ values of

cerussite are between 11.6 and 12.9 ‰, those of the limestone range from 22.9 to 24.1 ‰. Similarly, cerussite has low $\delta^{13}C$ values with a high variance (-11 to -15.1 ‰), while the $\delta^{13}C$ values of host carbonates are between -1.7 and 1.4 ‰.

Discussion

Significance of the different willemite generations

Textures support three successive generations of willemite, with differences in crystal shape, CL zoning and chemical composition. While idiomorphic Wil Ia is characterized by sector zoning, radial-fibrous aggregates of Wil Ib have oscillatory zoning and growth bands (Fig. 7). This textural evolution recalls that of the willemite from ore deposits in Namibia, Zambia (Terracciano 2008), or Belgium (Coppola et al. 2008), where two distinct forms of willemite agglomerates were distinguished. These authors described: 1) idiomorphic hexagonal crystals and 2) massive spheroids with radial-fibrous crystals, which are very similar to Wil Ia and Wil Ib observed at Bou Arhous, respectively. In the case of willemite, crystal shape is strongly controlled by temperature (Palache 1935; Pough 1941) and by the degree of supersaturation (Kostov 1968). Although accurate temperature constraints are missing, Kostov (1968) has proposed that, at high temperature, crystals are usually tabular and as temperature decreases, they tend to form elongated prisms along the c axis and, for extreme cases, radial agglomerates of fibers. Kostov (1968) also proposed that a slow crystallization from slightly supersaturated solutions could explain the short-prismatic to tabular habits.

373 Based on a detailed microscopic observation of ore samples, we established
374 the temporal sequence of mineralization at Bou Arhous (Fig. 9). Primary sulfide
375 mineralization follows or at least overlaps the dolomitization and the silicification.
376 The latter alteration is marked by the development of authigenic quartz crystals in the
377 micritic limestone. Such quartz is usually found in carbonates affected by saline or
378 hypersaline pore waters (Flügel 2010); at Bou Arhous, the pore waters, from which
379 the authigenic quartz crystals precipitated, may result from the influence of the
380 underlying Triassic evaporites (Leblanc 1968). Cerussite predates and postdates
381 willemite precipitation (Fig. 9), as it may be found as core inclusions and cementing
382 material (*e.g*. Figs. 4d and 5e). Intercalation of cerussite bands within growth-zoned
383 willemite (Fig. 5f) supports the contemporaneity of both phases. Dissolution of
384 willemite was probably caused by a change in the local hydrochemical conditions (*i.e*.
385 Si-undersaturated fluids, change of temperature) and resulted in the release of zinc
386 and silica into the solutions, contributing to either a precipitation of a new generation
387 of willemite (Wil II) or the formation of authigenic zinc clays (Buatier et al. 2016;
388 Choulet et al. 2016)
389
390 Incorporation of Ge in willemite with implications for cathodoluminescence
391 properties
392
393 Both EPMA and LA-ICPMS analyses indicate a variable Ge content in
394 willemite that may reach up to 1000 ppm (Table 2). These values are significantly
395 higher than those measured in the New Jersey deposits (less than 10 ppm; Höll et al.
396 2007) and in the Utah and New Mexico deposits (up to 350 ppm; Sheffer 1966), but
397 are comparable to those reported from the Tsumeb Ge deposit, Namibia (up to 1280

398 ppm; Lombaard et al. 1986) or Tres Marias Zn-Pb-(Ge) deposit, Mexico (up to 4000
399 ppm; Saini-Eidukat et al. 2009; 2016). The EPMA results of this study clearly show a
400 correlation with a negative slope between Si and Ge, explained by the Ge-Si
401 substitution within willemite (Figs. 8d and 8e). X-ray absorption fine structure
402 (XAFS) spectroscopy has confirmed that Ge in willemite occurs as Ge^{4+} (Melcher et
403 al. 2009; Saini-Eidukat et al. 2016). The lithophile behavior of germanium (Bernstein
404 1985), the short difference in ionic radii between Ge^{4+} (0.44 Å) and Si^{4+} (0.39 Å) and
405 the similarity of lattice parameters between Zn_2SiO_4 and Zn_2GeO_4 (Hang et al. 1970)
406 may explain the incorporation of Ge into willemite.
407 Generally, sulfide minerals like sphalerite (e.g. Cook et al. 2009; Bélissont et
408 al. 2014) and galena (Monteiro et al. 2006) may contain several thousands of ppm of
409 Ge. At Bou Arhous, the Ge content of the two sulfide minerals is below the detection
410 limit (100 ppm) of EPMA (Table 1), in agreement with the low Ge content of MVT
411 deposits (Höll et al. 2007). Although the limited amount of sphalerite and galena
412 relics precludes implication for the whole primary mineralization, it means that either
413 an exceptional secondary Ge enrichment is recorded within willemite or that the
414 sulfide minerals were not the source of Ge. Except for the Apex mine where Ge
415 grades (ca. 5000 ppm) in the weathering zone exceed those in the primary sulfides
416 (650 ppm; Bernstein 1986), the oxidation zones of Zn–Pb sulfide deposits are
417 generally depleted in Ge or at least not enriched (Höll et al. 2007). In the Tres Marias
418 Deposit (Saini-Eidukat et al. 2009), the Ge content of sphalerite averages 960 ± 515
419 ppm and is comparable to that of willemite (941 ± 89 ppm). Ge can be transported in
420 aqueous hydrothermal fluids as $Ge(OH)_4°(aq)$ at pH values <8 over a temperature
421 range of 20 to 350 °C (Pokrovsky et al. 2005). In addition, the solubility of Ge in
422 thermal waters increases with temperature and salinity (Melcher et al. 2003). In this

423 case, the source of Ge could be organic-rich rocks (e.g. black shale), which are
424 generally rich in Ge (Bernstein 1985) and are frequent in the Paleozoic basement of
425 Morocco (Lüning et al. 2000). Hydrothermal fluids would therefore be necessary to
426 introduce the Ge for the willemite.

427 In addition to Ge, willemite has a variable Pb content that may reach up to 2
428 wt%, similar to the contents measured in Tres Marias willemite (Saini-Eidukat et al.
429 2009). By plotting Pb versus Zn, a correlation with a negative slope between both
430 elements is given, suggesting the existence of a Zn-Pb substitution (Fig. 8f), also
431 reported by Saini-Eidukat et al. (2016). According to XAFS spectroscopy, Pb is
432 present as Pb^{2+} in willemite (Melcher et al. 2009; Saini-Eidukat et al. 2016).
433 Willemite containing ca. 0.5 wt% of Pb^{2+} was synthetized by the sol-gel method with
434 calcination at 1000°C (Yang et al. 2004). Trigonal willemite is characterized by Zn-O
435 bonds (Kostov 1968); as the difference between the ionic radii of Zn^{2+} (0.60 Å) and
436 Pb^{2+} (0.98 Å) is huge, only a limited amount of Pb^{2+} may be introduced, with strong
437 distortion of the tetrahedrally coordinated site. Alternatively, the ring crystal structure
438 of willemite is characterized by tessellated hollow hexagons made of Si and Zn
439 tetrahedrons (Klaska et al. 1978; Lukić et al. 2008), which may incorporate interstitial
440 ions like Pb^{2+} (Yang et al. 2004). The relative incompatibility of Pb in willemite is
441 also shown by the existence of orthorhombic larsenite (Palache 1928; Ito and Frondel
442 1967), $ZnPbSiO_4$, and the absence of solid solution between larsenite and willemite.
443 Hence, Saini-Eidukat et al. (2016) have proposed that Pb-rich willemite may contain
444 microdomains of larsenite. In case of Pb supersaturation conditions related to a
445 change of the fluid composition, secondary galena or cerussite may be precipitated
446 (Terracciano 2008), as illustrated by the cerussite and galena inclusions in willemite
447 cores (Figs. 4d and 4e) and the intercalated cerussite bands (Fig. 5f).

448 Correlations between the two substitutions (Zn-Pb and Si-Ge) can be
449 observed, depending on the willemite generations (Fig. 10). In the case of Wil Ia, all
450 data except those with low Pb and low Ge contents are distributed along a trending
451 curve with a negative slope, which tends toward the Pb-rich compositions of
452 willemite. This indicates that significant Ge amounts can be included in this particular
453 willemite generation, only if that latter one is poor in Pb. As the Pb content increases,
454 the Ge-Si substitution is much more limited, probably due to the distortion of the
455 tetrahedrally coordinated site caused by the introduction of large Pb^{2+} ions (Saini-
456 Eidukat et al. 2016). In contrast, for Wil Ib, the curve has a positive slope, suggesting
457 that there is no competition between the two substitutions (Fig. 10). This trend is
458 similar to that of Tres Marias willemite, which is also characterized by well-
459 developed oscillatory zoning (Saini-Eidukat et al. 2009; 2016). In the case of Wil II,
460 the small number of data and the low Ge content precludes discussing incorporation
461 mechanisms. The differences between Wil Ia and Wil Ib may be explained by the
462 variation of crystal shapes (prismatic versus fiber-like) and, in the case of Wil Ia, by
463 the development of peculiar faces, which may incorporate more or less Ge and Pb at
464 the their surface during crystallization. A similar mechanism has been proposed to
465 explain sectoral chemical (Ge, Ag) zoning in sphalerite (Barbanson and Geldron
466 1983). According to Pough (1940) and Kostov (1968), the main faces of willemite
467 prisms are {110}, {101}, {012} and {001}. While the first one is characteristic of
468 fibrous habits (e.g. Wil Ib), the three other one are frequent in prismatic crystals (e.g.
469 Wil Ia). The comparison of the surface atomic structure of the different faces shows
470 that all faces except {012} display alternating Zn and Si, with various Si/Zn ratios.
471 However, the {012} surface is a continuous plane of Si ions, which was much more
472 favorable for Ge incorporation. Therefore, the incorporation of Ge in Wil Ia is limited

473 by willemite crystal growth, while its introduction in Wil Ib depends on the chemical
474 composition of the fluids, which controls the element variation of oscillatory-zoned
475 crystals (Shore and Fowler 1996). Oscillatory growth zoning in willemite is
476 frequently described in the literature (Coppola et al. 2008; Terracciano 2008; Saini-
477 Eidukat et al. 2009; 2016), but it is the first time that sector zoning is reported for this
478 mineral. Growth sectors defined by the faces on which the growth took place are
479 characterized by variable Ge and Pb contents (Fig. 8). While Ge-rich bright sectors
480 {012} have low Pb contents, higher Pb concentration is found in Ge-poor dark sectors
481 {101}, {110} or {001}.

482 Spectral analysis curves are characterized by a maximum of intensity at 460-
483 480 nm (Fig. 11), in agreement with the blue luminescence observed under the
484 microscope (Fig. 6). The experimental curves from Bou Arhous willemite
485 significantly differ from those given by pure willemite (Randall 1938; Yang et al.
486 2004) or Mn-doped willemite (Leverenz 1950), but are very similar to that obtained
487 by analyzing synthetic Zn_2GeO_4 nanorods (Tsai et al. 2008). Zinc germanate has a
488 crystal structure similar to that of willemite (Hang et al. 1970). The obvious
489 correlation between the Ge content and the intensity of luminescence is only valid for
490 Wil Ia crystals and no similar observation was made for Wil Ib. Therefore, it is
491 difficult to ascertain the role of activator ion for Ge^{4+}. Alternative processes could be
492 envisaged: (i) quenching by ions with intense charge transfer bands like Fe^{2+}
493 (Terracciano 2008), (ii) sensitizing of Mn by ions with intensive absorption bands like
494 Pb^{2+} (Carpenter and Vicenzi 2012), (iii) luminescence caused by defect activators,
495 such as interstitial Pb^{2+} (Yang et al. 2004; Takahashi et al. 2010), or (iv) other
496 luminescence centers (e.g. Ti^{4+}, Eu^{2+}, Ce^{3+}, Hf^{4+}) not detected by the used analytical

497 methods, but recognized as activators for the blue luminescence (see a review in
498 Takesue et al. 2009).
499
500 Nature of the mineralizing fluids involved
501
502 The host rock carbonates of the Bou Arhous mineralization have $\delta^{13}C$ values
503 in a range from -1.7 to 1.4 ‰ (Table 3), similar to those of Pliensbachian limestone
504 (0.5 to 2.9 ‰) hosting the Bou Dahar Zn-Pb mineralization, 75 km to the west of Bou
505 Arhous (Rddad and Bouhlel 2016). The $\delta^{18}O$ values of carbonates (22.9 to 24.1 ‰)
506 are also similar to those of Bou Dahar (22.7 to 25.7 ‰). Such $\delta^{13}C$ and $\delta^{18}O$ values
507 are within the range of marine Jurassic limestones (Veizer and Hoefs 1976).
508 Carbon stable isotope ratios of cerussite are similar to those measured for
509 supergene ores from Iglesiente, Broken Hill and deposits in Eastern Belgium (see a
510 review in Gilg et al. 2008; Fig. 12a). The $\delta^{13}C$ (between -11 and -15.1 ‰) values are
511 lower than the typical values of cerussite from marine slags (0 ± 2‰) given by Gilg
512 et al. (2008). The ^{13}C-depleted carbon component can be explained by either
513 contributions of carbon from soil CO_2 related to respiration of C3 plants (Cerling
514 1984) or organic carbon issued from the activity of sulfide-oxidation bacteria
515 (Melchiorre and Enders 2003). The average $\delta^{18}O$ value (12.1 ‰, n = 4) of cerussite is
516 lower than that obtained in supergene deposits (15 to 20 ‰) or from marine slags
517 (17.9 ‰, Gilg et al. 2008), but similar to that of the Garpenberg deposit, Sweden
518 (11.6 ‰; Vivallo and Broman 1993) or to that of Badenweiler in the Schwarzwald
519 mining district (11.2 to 15.6 ‰, Hassler et al. 2014). These low values may be
520 explained by either isotopically lighter water or by higher temperatures of formation.
521 The absence of any correlation between carbon and oxygen isotope values of cerussite

522 suggests that dissolution of the host limestone cannot only account for the source of
523 carbonate in cerussite.

524 At present, the oxygen isotope composition of willemite was only reported
525 from Sterling Hill (USA) and Vazante (Brazil), with respective isotopic compositions
526 between 7.4 ‰ and 11.4 ‰ and between 10.9 ‰ to 13.8 ‰ (Johnson et al. 1990;
527 Monteiro et al. 1999). In addition to fluid inclusions that recorded salinities of 3-15
528 wt% eq. NaCl and homogenization temperatures between 120 and 175°C (Dardenne
529 and Freitas-Silva 1999), Monteiro et al. (1999) recalculated a temperature range (from
530 263 to 294°C) at the time of mineralization using the stable isotope composition of
531 cogenetic mineral pairs. Therefore they recalculated the oxygen isotope composition
532 of the fluid in equilibrium with willemite, using the theoretical fractionation equation
533 between willemite and water (Zheng 1993).

534

535 $1000\ln\alpha_{wil\text{-}wat} = 3.79(10^6/T^2) - 8.94(10^3/T) + 2.5$ (*eq. 1*)

536

537 The range of oxygen isotope compositions ($\delta^{18}O$ = 12 to 14 ‰) of the fluid (Fig. 12b)
538 led Appold and Monteiro (2009) to propose a mixing process between hot, saline,
539 reducing, acidic fluids and cool, oxidizing meteoric waters; precipitation results from
540 an increase in pH and/or a small decrease in the temperature (Brugger et al. 2003).
541 Mixing of hydrothermal fluids with seawater was also hypothesized for explaining the
542 isotopic compositions of Sterling Hill rocks and ores (Johnson et al. 1990).

543 The oxygen isotope composition of Bou Arhous willemite is characterized by
544 $\delta^{18}O$ values ranging between 5.3 and 7.8 ‰ (Table 3), significantly lower than those
545 measured for Vazante or Sterling Hill. The large range of oxygen isotope values (2.5
546 ‰) may also indicate that fluid mixing was involved during the precipitation of

willemite or that willemite precipitated at different temperatures. The study of fluid inclusions in willemite from Bou Arhous was not conclusive, with only monophase inclusions observed. This suggests that the temperatures of the Tertiary fluids responsible for willemite formation was below 130°C (e.g. Gilg et al. 2014). The established paragenetic succession shows a first-order contemporaneity of willemite and cerussite (Fig. 9). Using equation (*eq. 1*) and the oxygen isotope fractionation equation between cerussite and water (*eq. 2*; Gilg et al. 2008), it is possible to calculate the equilibrium temperature between the willemite-cerussite pairs (BA117, BA118 and BA134).

$$1000\ln\alpha_{cer\text{-}wat} = 2.29(10^6/T^2)-3.56 \qquad (eq.\ 2)$$

After discarding the negative solutions, the obtained temperatures range from 237 to 343°C. While these temperatures are similar to those proposed in hypogene willemite deposits (e.g. Vazante; Monteiro et al. 1999), the local geological setting of Bou Arhous deposit totally differs from the structural and paragenetic characteristics of hypogene deposits, without carbonatization and hematite alteration (Hitzman et al. 2003). In addition, such temperatures are too high for cerussite, a mineral exclusively reported in the supergene stages of ore deposits, although high temperature (up to 240 °C) experiments on cerussite were made by O'Neil et al. (1969). Cerussite and willemite are not in isotopic equilibrium and thus not cogenetic. They precipitated from at least two fluids with different oxygen isotope compositions or formed at different temperatures. The successive bands of cerussite and willemite (Fig. 5f) rather support the hypothesis of different fluids involved in the precipitation of both minerals.

572

573 Supergene versus low-temperature hypogene willemite

574

575 Based on the present data, it is not possible to ascertain the origin of willemite
576 at Bou Arhous. The geological features of the deposits suggest a supergene origin of
577 the non-sulfide mineralization and therefore low temperatures (around 25 °C) could
578 be assumed. Such a temperature corresponds to that presently recorded in the karst
579 cavities hosting the mineralization. Synthetic willemite was obtained at room
580 temperature by sol-gel methods and occurs as small spheres or aggregates (Esquevin
581 1960; Takesue et al. 2009). Thermodynamic modeling also showed that willemite
582 may form at 25 °C under high pH, high silica activity and low CO_2 partial pressure
583 conditions (Brugger et al., 2003). The oxygen isotopic composition of the paleowater
584 was calculated at 25 °C, using the bond-strength theory equation for isotope
585 fractionation between willemite and water (eq. 1; Zheng 1993). The obtained isotopic
586 compositions for the paleowater (Table 3) plot close to the meteoric line (Craig 1961),
587 although no constrain on the vertical axis (δD) is available (Fig. 12b). The computed
588 $\delta^{18}O$ values for the paleofluid have a range between -9.3 ‰ and -7.4 ‰ (Table 3),
589 lower than the average value (-7.5 ‰) of present-day precipitations at Bab Bou Idir,
590 northern Morocco (Ouda et al. 2005). This difference could be explained by
591 differences in altitude and climate between the Bab Bou Idir station and the Bou
592 Arhous range during the Tertiary.

593 Alternatively, low-temperature hydrothermal fluids (<130°C) may have been
594 involved in the formation of willemite. Such fluids have been hypothesized for the
595 origin of willemite in the deposits of Eastern Belgium (Coppola et al. 2008). In the
596 case of Bou Arhous, the absence of isotopic equilibrium between cerussite and

willemite and the relatively large range of isotopic compositions for willemite suggest the involvement of at least two fluids and their mixing. Together with supergene water, hydrothermal fluids have also contributed to the formation of the non-sulfide ore. As temperature is the main parameter controlling the precipitation of willemite instead of hemimorphite (McPhail et al. 2003, 2006), temperatures over 90-100 °C are required, in agreement with the presence of monophase inclusions (T <130 °C). Assuming a temperature of 100 °C, we recalculated a range of isotopic compositions for the paleofluid between -0.5 and 2 ‰ (Table 3). The data fall into an intermediate domain between the deep fluid fields and the supergene line, in agreement with the mixing hypothesis (Fig. 12b).

Whatever the hypothesis, high silica activity is necessary to prevent the precipitation of smithsonite and hydrozincite, which are only reported in few samples in the Bou Arhous deposit (Leblanc 1968). The source of silica is thus a crucial issue. Like in Eastern Belgium (Coppola et al. 2008), few present-day hot springs are currently known in the area, especially to the west of Bou Arhous (Bahaj et al. 2013). In addition, the hydrochemical study of the underground waters in the Zizi and Guir basins, to the south of the Bou Arhous range, shows that the present-day water within the Sinemurian limestone is a calcic bicarbonate type; their extremely high silica content (up to 5000 mg/L) are interpreted as the result of a long residence time of the waters and/or an important mixture with thermal waters (Bahaj et al. 2013). A local source for silica cannot be excluded too, and may even be indicated by the partial dissolution of the idiomorphic quartz crystals present in the micritic limestone (Fig. 3). Although the dissolution rate of quartz is low at low temperatures (Dove 1994), long-lived weathering since the Tertiary and undersaturation of the karst waters may partly contribute to a slow but non-negligible enrichment in silica. An alternative

622 local source of Si could be the residual clays of the karst, mainly composed of illite,
623 kaolinite and smectite (Buatier et al. 2006; Choulet et al. 2016).
624
625 **Conclusion**
626
627 The Bou Arhous deposit in the Moroccan High Atlas is characterized by
628 willemite ore. Several generations of willemite spatially and temporally associated
629 with cerussite were distinguished based on different criteria including crystal shape,
630 zoning type and major and trace element contents. Based on oxygen stable isotope
631 data of bulk mineral fractions, cerussite and willemite are not in isotope equilibrium
632 and therefore were not cogenetic, requiring different fluid compositions for their
633 formation. In addition to a contribution of supergene water, low-temperature (<130
634 °C) hydrothermal fluids buffered by the country rocks may have been involved. The
635 input of hydrothermal fluids is probably responsible for the high silica activity, which
636 is necessary to precipitate willemite instead of zinc carbonates, especially within
637 carbonate host rocks. A local contribution by the silicate minerals of the host
638 limestone cannot be excluded though. Further work on willemite is required to verify
639 the conditions of formation; stable oxygen isotopes compositions of the different
640 generations of willemite and cerussite could help to understand the evolution of
641 mineralizing fluids.
642 The Bou Arhous willemite may contain up to several thousands ppm of Ge.
643 The Ge content in willemite, related to the Si-Ge substitution, is controlled by the
644 crystal morphology in the case of sector zoning. Since the Ge content of sulfide
645 minerals is low (less than 100 ppm), it is hypothesized that hydrothermal fluids,
646 responsible for the formation of willemite, also transported Ge in part. In the present

context of Ge criticality, willemite ores may therefore represent an interesting target for exploration (Höll et al. 2007; EU Commission 2014).

Acknowledgments

The authors are indebted to Managem Company for providing access to the Bou Arhous Mine. They thank Didier Convert-Gaubier for thin-section preparation, as well as Aurélien Eglinger and Philippe Goncalves from Chrono-Environnement for LA-ICPMS data acquisition and Martin Robyr, Evelyne Tornare and Anne-Cécile Hauser from University of Lausanne for EPMA data acquisition. They also warmly acknowledge the assistance of Benita Putlitz with oxygen isotope measurements on the silicate line at UNIL. This study has benefited from a financial support by of Région Franche-Comté with the 2014 "Argzinc" Franco-Suisse project. Access to SEM facilities of the MIMENTO center was made in the frame of cooperative projects in the Renatech network. Two anonymous reviewers, Associate Editor Albert Gilg and Editor-in-Chief Bernd Lehmann are acknowledged for their constructive remarks that helped to improve the manuscript.

Figure captions

Table 1 WDS results of the primary sulfide minerals (sphalerite and galena). Detection limits (in ppm): S (320), Cd (100), As (210), Bi (900), Fe (110), Ag (460), Ni (120), Zn (330), Pb (720), Ge (100), Cu (110). Avg: average, SD: standard deviation, RSD: relative standard deviation (RSD = (SD/Avg.) * 100), n: number of analyses, (-): values below the detection limit.

672

673 Table 2 WDS analyses (oxide in weight percent) and LA-ICPMS results (in ppm) of
674 the different willemite generations described in the text. Detection limits (in ppm): Ge
675 (84), Al (64), Pb (454), Cd (105), Fe (237), Ca (120), Mn (336). Avg: average, SD:
676 standard deviation, RSD: relative standard deviation (RSD = (SD/Avg.) * 100), n:
677 number of analyses, (n.d.): values below the detection limit.

678

679 Table 3 Stable isotope (C, O) compositions measured for cerussite, willemite and host
680 limestone from the Bou Arhous deposit. For willemite, the oxygen isotopic
681 composition of the fluid ($\delta^{18}O$ $VSMOW_f$) was calculated with the fractionation
682 equation from Zheng (1993), assuming temperatures of 25 ([1]) and 100°C ([2]).

683

684 Figure 1 **a** Map of northwestern Africa, illustrating the location of the Bou Arhous
685 deposits with respect to the major tectonic features. **b** Cross-section of the Bou
686 Arhous deposit, showing the faulted anticline (adapted from Leblanc 1968). Triassic
687 rocks (t) are covered by Lower Jurassic rocks (l_1 to l_4). The mine, made up of 4 levels
688 (from level 0 to level 100) is hosted in massive limestone, to the south of the fault and
689 mainly exposes a non-sulfide mineralization.

690

691 Figure 2 **a** Field image of the reddish thin-bedded folded limestone that alternates
692 with marl. **b** General view of the southern flank of the Jbel Bou Arhous showing
693 cavities originally filled by non-sulfide mineralization (Choulet et al. 2014). **c** and **d**
694 Mine outcrops showing the “black ore” composed of galena and willemite, associated
695 with zinc clays, detrital clays or hydrozincite.

696

Figure 3 Cathodoluminescence images of the host limestone. **a** Micrite (yellowish pink) enclosing idiomorphic and partly dissolved quartz (blue), with locally secondary sparite (yellow). **b** Dolomite (reddish pink) pervading into the micrite (yellowish brown) and locally transformed into sparite (yellow). **c** Small sinkhole formed after the dissolution of micrite (brown) and filled by sparite (yellow). Note the accumulation of euhedral crystals of dolomite (pink) and quartz (blue) at the bottom of the cavity.

Figure 4 Images of the ore mineralization. **a** General view (TL, nic+) of the willemite (Wil) ore including relics of sphalerite (Sp) (Sample BA06C). **b** BSE image of (a) showing sphalerite relic rimmed by secondary galena (Gn II), within willemite. Note the idiomorphic quartz (Qz) crystals, partly corroded and fractured. **c** BSE image of primary galena (Gn I) coated by a thin rim of anglesite (Ang) itself transformed into cerussite (Cer I) (Sample BA05A). **d** (TL, nic+) and **e** (RL, nic//) Aggregates of galena and cerussite (Cer I + Gn I) included within elongated willemite (Wil) crystals (Sample BA06B). Large crystal of cerussite (Cer III) devoid of galena inclusions fills the porosity between the willemite (Wil) aggregates. **f** (TL, nic+), **g** (TL, nic//) and **h** (RL, nic//) Thin and tabular barite (Brt) crystals associated with willemite (Wil), late cerussite (Cer III) and sphalerite (Sp), rimmed by secondary galena (Gn II) (Sample BA06A). TL: transmitted light, BSE: backscattered elelectron, RL: reflected light, nic+: crossed nicols, nic//: parallel nicols.

Figure 5 **a** Aggregate of willemite spherulites in the massive ore facies (TL, nic+) (Sample BA135F). **b** (TL, nic+) and **c** (BSE image) Association of willemite with newly formed zinc clays and detrital quartz, extensively described in Choulet et al.

(2016) (Sample BA130F). **d** (TL, nic+) and **e** (RL, nic//) General view of the different generations of cerussite and relationships with the willemite spherulite (Sample BA05B). **f** BSE image illustrating willemite spherulites postdating early cerussite (cer I associated with primary galena relic) and predating late cerussite (cer III). Note the cerussite band (cer II) intercalated during the growth of the spherulite. See Figure 4 for abbreviations.

Figure 6 Secondary electron images of separated willemite crystals, showing idiomorphic barrel shape (**a**) (Sample BA124), twinning (**b**) (Sample BA133), and radial-fibrous distribution (**c** and **d**) (Sample 134).

Figure 7 Cathodoluminescence images of the willemite ore. **a** Barrel-shaped crystals showing a 1) core of Wil Ia with sector zoning and 2) a rim of Wil Ib with oscillatory zoning (Sample BA130). **b** willemite spherulite composed by a core of Wil Ia mainly composed of dark sectors, rimmed by oscillatory-zoned Wil Ib (Sample BA135F). **c** aggregated spherulites showing a well developed Wil Ib stage (Sample BA128F). Note the cerussite veins (bright white-blue) that crosscut Wil Ia and partly Wil Ib. **d** Small crystals of late willemite (Wil II) filling the porosity between early willemite (Wil Ia and Wil Ib) (BA135). **e** Partly dissolved willemite, exposing relics of an oscillatory-zoned rim and dark sectors within the core. The bright zone in the center is due to early cerussite (Sample BA128F). **f** Partly dissolved willemite spherulite crosscut by cerussite veinlets (bright white-blue). Note on the upper right corner that the sequence is probably repeated with time, as unaltered willemite with oscillatory zoning overgrows on the dissolved spherulites (Sample BA128F).

747 Figure 8 Cathodoluminescence images of the willemite crystals, showing the location
748 of *in situ* point analyses by LA-ICPMS (**a** and **b**) and by EPMA (**c**). **d** Ge versus Si
749 plot of individual EPMA analyses located in fig. 8c. **e** Ge versus Si plot of all EPMA
750 analyses, including the distinguished willemite generations. **f** Pb versus Zn plot of all
751 EPMA analyses, including the distinguished willemite generations. The number of
752 Ge, Si, Zn and Pb moles was calculated from the weighted percent oxide
753 compositions reported in Table 2.
754
755 Figure 9 Synthetic paragenetic sequence of the observed minerals at the Bou Arhous
756 deposit. Vertical lines represent the limits between the different steps that contribute
757 to the present-day mineralization. Thickness of the horizontal line corresponds to the
758 relative abundance of each mineral species.
759
760 Figure 10 Ge/(Ge+Si) versus Pb/(Pb+Zn) plot illustrating that the two substitutions
761 (Ge-Si and Pb-Zn) are variably correlated depending on the willemite generation. The
762 data from willemite of Tres Marias deposit, Mexico (Saini-Eidukat et al. 2009) are
763 reported for comparison; these latter data show a trend similar to that of Wil Ib from
764 Bou Arhous.
765
766 Figure 11 Luminescence spectra of two observed areas dominated by Wil Ia or Wil
767 Ib. The curves of variously Mn-doped willemite (Leverenz 1950) and of a synthetic
768 Ge analog of willemite (Zn_2GeO_4, Tsai et al. 2008) are shown for comparison.
769
770 Figure 12 **a** Carbon and oxygen isotope compositions of cerussite and host limestone
771 from the Bou Arhous deposit. Data from other deposits are taken from Gilg et al.

772 (2008) and references herein. **b** Hydrogen and oxygen isotope compositions of
773 supergene (25 °C) and low-temperature (100 °C) hydrothermal fluids in equilibrium
774 with Bou Arhous willemite. The isotope composition of fluids in equilibrium with
775 hypogene willemite from Vazante, Brazil (Monteiro et al. 1999) is shown for
776 comparison.
777
778 **References**
779
780 Appold MS, Monteiro LVS (2009) Numerical modeling of the hydrothermal zinc
781 silicate and sulfide mineralization in the Vazante deposit, Brazil. Geofluids 9:96–115
782
783 Bahaj T, I. Kacimi I, Hilali M, Kassou N, Mahboub A (2013) Preliminary study of the
784 groundwater geochemistry in the sub-desert area in Morocco: case of the Ziz-Ghris
785 basins. Proced Earth Planet Sci 7:44–48
786
787 Barbanson L, Geldron A (1983) Distribution du germanium, de l'argent et du
788 cadmium entre les schistes et les minéralisations stratiformes et filoniennes à blende-
789 sidérite de la region de Saint-Salvy (Tarn). Chron Rech Min 470:33–42
790
791 Belissont R, Boiron M-C, Luais B, Cathelineau M (2014) LA-ICP-MS analyses of
792 minor and trace elements and bulk Ge isotopes in zoned Ge-rich sphalerites from the
793 Noailhac – Saint-Salvy deposit (France): Insights into incorporation mechanisms and
794 ore deposition processes. Geochim Cosmochim Acta 126:518–540
795

796 Bernstein LR (1985) Germanium geochemistry and mineralogy. Geochim
797 Cosmochim Acta 49:2409-2422
798
799 Bernstein LR (1986) Geology and mineralogy of the APEX germanium–gallium
800 mine, Washington County, Utah. US Geol Surv Bull 1577:1–9
801
802 Bhalla RJRSB, White EW (1972) Cathodoluminescence characteristics of Mn^{2+}
803 activated willemite (Zn_2SiO_4) single crystals . J Electrochem Soc 119:740–743
804
805 Boni M, Large DE (2003) Nonsulfide zinc mineralization in Europe: an overview.
806 Econ Geol 98:715–729
807
808 Boni M, Mondillo N (2015) The "calamines" and the "others": the great family of
809 supergene nonsulfide zinc ores. Ore Geol Rev 67:208– 233
810
811 Boni M, Coppola V, Dejonghe L, Fedele L (2005) Willemite in the Belgian non-
812 sulphide deposits: a fluid inclusion study. Period Miner 73:1–14
813
814 Boni M, Gilg HA, Balassone G, Schneider J, Allen CR, Moore F (2007) Hypogene
815 Zn carbonate ores in the Angouran deposit, NW Iran. Mineral Deposita 42:799–820
816
817 Boni M, Terracciano R, Balassone G, Gleeson SA, Matthews A (2011) The
818 carbonate-hosted willemite prospects of the Zambezi Metamorphic Belt (Zambia).
819 Mineral Deposita 46:707–729
820

821 Brugger J, McPhail DC, Wallace M, Waters J (2003) Formation of willemite in
822 hydrothermal environments. Econ Geol 98:819–835
823
824 Buatier M, Choulet F, Petit S, Chassagnon R, Vennemann T (2016) Nature and origin
825 of natural Zn clay minerals from the Bou Arhous Zn ore deposit: Evidence from
826 electron microscopy (SEM-TEM) and stable isotope compositions (H and O). App
827 Clay Sci, DOI: 10.1016/j.clay.2016.07.004
828
829 Carpenter P, Vicenzi E (2012) A combined EPMA and cathodoluminescence study of
830 minerals from Franklin NJ. Microsc Microanal 18(S2):1746–1747
831
832 Cerling TE (1984) The stable isotopic composition of modern soil carbonate and its
833 relationship to climate. Earth Planet Sci Letts 71:229–240
834
835 Charles N, Choulet F, Sizaret S, Chen Y, Barbanson L, Ennaciri A, Badra L, Branquet
836 Y (2016) Internal structures and dating of non-sulphide Zn deposits using rock
837 magnetism: insights from the Moroccan High Atlas. Mineral Deposita 51:151–175
838
839 Choulet F, Charles N, Barbanson L, Branquet Y, Sizaret S, Ennaciri A, Badra L, Chen
840 Y (2014) Non-sulfide zinc deposits of the Moroccan High Atlas: multi-scale
841 characterization and origin. Ore Geol Rev 56:115–140
842
843 Choulet F, Buatier M, Barbanson L, Guégan R, Ennaciri A (2016) Zinc-rich clays in
844 supergene non-sulfide zinc deposits. Mineral Deposita 51:467-490
845

Cook NJ, Ciobanu CL, Pring A, Skinner W, Shimizu M, Danyushevsky L, Saini-Eidukat B, Melcher F (2009) Trace and minor elements in sphalerite: a LA-ICPMS study. Geochim Cosmochim Acta 73:4761–4791

Coppola V, Boni M, Gilg HA, Balassone G, Dejonghe L (2008) The "calamine" nonsulfide Zn–Pb deposits of Belgium: petrographical, mineralogical and geochemical characterization. Ore Geol Rev 33: 187–210

Craig H (1961) Isotopic variations in meteoric waters. Science 133:1702–1703

Daliran F, Pride K, Walther J Berner ZA Bakker RJ (2013) The Angouran Zn (Pb) deposit, NW Iran: evidence for a two stage, hypogene zinc sulfide–zinc carbonate mineralization. Ore Geol Rev 53:373–402

Dardenne MA, Freitas-Silva FH (1999) Pb-Zn ore deposits of Bambuí and Vazante groups, in the São Francisco Craton and Brasília Fold Belt, Brazil. In: Silva MG, Misi A (eds) Base metal deposits of Brazil. MME7CPRM/DNPM, Belo Horizonte, pp. 75-83

Dejonghe L (1998) Zinc-lead deposits of Belgium. Ore Geol Rev 12:329–354

Dove PM (1994) The dissolution kinetics of quartz in sodium chloride solutions at 25 degrees to 300 degrees C. Am J Sci 294:665–712

870 Esquevin J (1960) Les silicates de zinc, étude de produits de synthèse et des minéraux
871 naturels. Institut National de la Recherche Agronomique, Saint-Amand (in French)
872
873 EU Commission (2014) Critical raw materials for the EU. Report of the Ad-hoc
874 Working Group on Defining Critical Raw Materials. Brussels, Belgium
875
876 Flügel E (2010) Microfacies of Carbonate Rocks, 2nd edn. Springer-Verlag, Berlin-
877 Heidelberg
878
879 Frizon de Lamotte D, Saint-Bezar B, Bracene E, Mercier E (2000) The two main
880 steps of the Atlas building and geodynamics of the western Mediterranean. Tectonics
881 19:740–761
882
883 Gilg HA, Struck U, Vennemann T, Boni M (2003) Phosphoric acid fractionation for
884 smithsonite and cerussite between 25 and 72 °C. Geochim Cosmochim Acta 67:4049–
885 4055
886
887 Gilg HA, Boni M, Hochleitner R, Struck U (2008) Stable isotope geochemistry of
888 carbonate minerals in supergene oxidation zones of Zn–Pb deposits. Ore Geol Rev
889 33:117–133
890
891 Gilg HA, Krüger Y, Taubald H, van den Kerkhof AM, Frenz M, Morteani G (2014)
892 Mineralisation of amethyst-bearing geodes in Ametista do Sul (Brazil) from low-
893 temperature sedimentary brines: evidence from monophase liquid inclusions and
894 stable isotopes. Miner Deposita 49:861-877

895

896 Groves I, Carman CE, Dunlap WJ (2003) Geology of the Beltana willemite deposit,
897 Flinders Ranges, South Australia. Econ Geol 98:797–818

898

899 Hang C, Simonov MA, Belov NV (1970) Crystal structures of willemite $Zn_2(SiO_4)$
900 and its germanium analog $Zn_2(GeO_4)$. Sov Phys Crystallogr USSR 15:387–390

901

902 Hassler K, Taubald H, Markl G (2014) Carbon and oxygen isotope composition of
903 Pb-, Cu- and Bi-carbonates of the Schwarzwald mining district: Carbon sources, first
904 data on bismutite and the discovery of an oxidation zone formed by ascending thermal
905 water. Geochim Cosmochim Acta 113:1–16

906

907 Hitzman MW, Reynolds NA, Sangster DF, Allen CR, Carman CE (2003)
908 Classification, genesis, and exploration guides for nonsulfide zinc deposits. Econ
909 Geol 98:685–714

910

911 Höll R, Kling M, Schroll E (2007) Metallogenesis of germanium - A review. Ore
912 Geol Rev 30:145–180

913

914 Ito J, Frondel C (1967) Synthesis of lead silicates: larsenite, barysilite and related
915 phases. Am Mineral 52:1077-1084

916

917 Johnson CA, Rye DM, Skinner BJ (1990) Petrology and stable isotope geochemistry
918 of the metamorphosed zinc-iron-manganese deposit at Sterling Hill, New Jersey:
919 Econ Geol 85:1133–1161

Kasemann S, Meixner A, Rocholl A, Vennemann T, Schmitt A, Wiedenbeck M (2001) Boron and oxygen isotope composition of certified reference materials NIST SRM 610/612, and reference materials JB-2G and JR-2G. Geostand Newsl 25:405–416

Klaska K-H, Eck JC, Pohl D (1978) New investigation of willemite. Acta Crystallogr B34:3324–3325

Kostov I (1968) Habit types and genesis of phenakite and willemite. Krist Techn 3: 629–636

Laville E, Piqué A (1991) La distension crustale atlantique et atlasique au Maroc au début du Mésozoïque: le rejeu des structures hercyniennes. Bull Soc Geol Fr 162:1161–1171

Leblanc M (1968) Étude géologique et métallogénique du Jbel Bou-Arhous et de son prolongement oriental (Haut Atlas marocain oriental). Not Mem Serv Geol Maroc 206:117–206

Leverenz HW (1950) An introduction to luminescence of solids. John Wiley & Sons, NewYork

Lombaard AF, Günzel A, Innes J, Krüger TL (1986) The Tsumeb lead-copper-zinc-silver deposit, south west Africa/Namibia. In: Anhaeusser CR, Maske S (eds) Mineral

945 Deposits of Southern Africa. Geological Society of South Africa, Johannesburg, pp
946 1761–1787
947
948 Lukić DM, Petrović, Dramićanin MD, Mitrić M, Đaćanin L (2008) Optical and
949 structural properties of $Zn_2SiO_4:Mn^{2+}$ green phosphor nanoparticles obtained by a
950 polymer-assisted sol–gel method. Scr Mater 58:655-658
951
952 Lüning S, Loydell DK, Sutcliffe O, Ait Salem A, Archer R, Zanella E, Craig J, Harper
953 DAT (2000): Silurian - Lower Devonian black shales in Morocco: Where are the
954 organically richest horizons? J Petrol Geol 23:293-311
955
956 McPhail DC, Summerhayes E, Welch S, Brugger J (2003) The geochemistry of zinc
957 in the regolith. In: Roach IC (ed) Advances in Regolith. CRC for Landscape
958 Environments and Mineral Exploration, pp. 287–291
959
960 McPhail DC, Summerhayes E, Jayaratne V, Christy A (2006) Hemimorphite
961 solubility and stability of low-T zinc minerals. Geochim Cosmochim Acta 70:A414
962
963 Melcher F, Saini-Eidukat B, Göttlicher J, Steininger R, Cook N, Ciobanu C (2009)
964 Germanium in sphalerite and willemite at the Tres Marias mine, Mexico: An EMPA,
965 CL, LA-ICP-MS and synchrotron study. In: Hallesches Jahrbuch für
966 Geowissenschaften. DMG-Tagung 2009, Halle, pp. 163
967

968 Melchiorre EB, Enders MS (2003) Stable isotope geochemistry of copper carbonates
969 at the Northwest Extension deposit, Morenci district, Arizona: implications for
970 conditions of supergene oxidation and related mineralization. Econ Geol 98:607–621
971
972 Monteiro LVS, Bettencourt JS, Spiro B, Graca R, Oliveira TF (1999) The Vazante
973 zinc mine, Minas Gerais, Brazil: constraints on willemitic mineralization and fluid
974 evolution: Explor Min Geol 8:21–42
975
976 Monteiro LVS, Bettencourt JS, Juliani C, Oliveira TF (2006) Geology, petrography,
977 and mineral chemistry of the Vazante non-sulfide and Ambrosia and Fagundes
978 sulfide-rich carbonate-hosted Zn-(Pb) deposits, Minas Gerais, Brazil. Ore Geol Rev
979 28:201–234
980
981 Monteiro LVS, Bettencourt JS, Juliani C, Oliveira TF (2007) Nonsulfide and sulfide-
982 rich zinc mineralizations in the Vazante, Ambrosia and Fagundes deposits, Minas
983 Gerais, Brazil: Mass balance and stable isotope characteristics of the hydrothermal
984 alterations. Gondwana Res 11:362–381
985
986 Mouguina EM (2004) Les minéralisations polymétalliques (Zn–Pb, Cu, Co, Ni) du
987 Jurassique du Haut Atlas central (Maroc): Contexte géodynamique, typologies et
988 modèles génétiques. Dissertation, Faculté des Sciences Semlalia de Marrakech
989
990 O'Neil JR, Clayton RN, Mayeda TK (1969) Oxygen isotope fractionation in divalent
991 metal carbonates. J Chem Phys 51:5547-5558
992

993 Ouda B, El Hamdaoui A, Ibn Majah M (2005) Isotopic composition of precipitation at
994 three Moroccan stations influenced by oceanic and Mediterranean air masses. In:
995 Isotopic composition of precipitation in the Mediterranean Basin in relation to air
996 circulation patterns and climate. IAEA, Vienna, TECDOC-1453 pp 125-140
997
998 Palache C (1928) Phosphorescence and fluorescence of Franklin minerals. Am
999 Mineral 13:330–333
1000
1001 Palache C (1935) The minerals of Franklin and Sterling Hill, Sussex County, New
1002 Jersey. US Geol Surv Prof Pap 180, USGS, Washington
1003
1004 Pearce NJG, Perking WT, Westgate JA, Gorton MP, Jackson SE, Neal CR, Chenery
1005 SP (1997) A compilation of new and published major and trace element data for NIST
1006 SRM 610 and NIST SRM 612 glass materials. Geostand Newsl 21:115–144
1007
1008 Pokrovski GS, Roux J, Hazemann J-L, Testemale D (2005) An X-ray absorption
1009 spectroscopy study of argutite solubility and germanium aqueous speciation in
1010 hydrothermal fluids to 500 °C and 400 bar. Chem Geol 217:127-145
1011
1012 Pough FH (1940) Willemite morphology and paragenesis at Balmat, New York. Am
1013 Mineral 25:488-496
1014
1015 Pough FH (1941) Occurrence of willemite. Am Mineral 26:92–102
1016
1017 Randall JT (1938) Luminescence of solids at low temperatures. Nature 142:113–114

1018

1019 Rddad L, Bouhlel S (2016) The Bou Dahar Jurassic carbonate-hosted Pb-Zn-Ba
1020 deposits (Oriental High Atlas, Morocco): Fluid-inclusion and C-O-S-Pb isotope
1021 studies. Ore Geol Rev 72:1072–1087

1022

1023 Reichert J, Borg G (2008) Numerical simulation and a geochemical model of
1024 supergene carbonate-hosted non-sulphide zinc deposits. Ore Geol Rev 33:134–151

1025

1026 Rosenbaum J, Sheppard SMF (1986) An isotopic study of siderites, dolomites and
1027 ankerites at high temperatures. Geochim Cosmochim Acta 50:1147–1150

1028

1029 Rouvier H, Perthuisot V, Mansouri A (1985) Pb-Zn deposits and salt-bearing diapirs
1030 in Southern Europe and North Africa. Econ Geol 80:666–687

1031

1032 Saini-Eidukat B, Melcher F, Lodziak J (2009) Zinc-germanium ores of the Tres
1033 Marias mine, Chihuahua, Mexico. Mineral Depos 44:363–370

1034

1035 Saini-Eidukat B, Melcher F, Göttlicher J, Steininger R (2016) Chemical environment
1036 of unusually Ge- and Pb- rich willemite, Tres Marias Mine, Mexico. Minerals 6:20,
1037 doi:10.3390/min6010020

1038

1039 Sheffer HW (1966) The occurrence of germanium in willemite. Geochim Cosmochim
1040 Acta 30:837–838

1041

1042 Shore M, Fowler, AD (1996) Oscillatory zoning in minerals: A common
1043 phenomenon. Can Mineral 34:1111–1126
1044
1045 Spötl C, Vennemann TW (2003) Continuous-flow isotope ratio mass spectrometric
1046 analysis of carbonate minerals. Rapid Commun Mass Spectrom 17:1004–1006
1047
1048 Swart PK, Burns SJ, Leder JJ (1991) Fractionation of the stable isotopes of oxygen
1049 and carbon during reaction of calcite with phosphoric acid as a function of
1050 temperature and method. Chem Geol 86:89–96
1051
1052 Takahashi Y, Ando M, Iwasaki K, Masai H, Fujiwara T (2010) Defect activation in
1053 willemite-type Zn2GeO4 by nanocrystallization. Appl Phys Lett. doi:
1054 10.1063/1.3481081
1055
1056 Takesue M, Hayashi H, Smith RL (2009) Thermal and chemical methods for
1057 producing zinc silicate (willemite): A review. Prog Cryst Growth Char Mat 55:98–
1058 124
1059
1060 Terracciano R (2008) Willemite mineralisation in Namibia and Zambia. Dissertation,
1061 Università degli Studi di Napoli Federico II
1062
1063 Tsai MY, Yu CY, Wang CC, Perng TP (2008) Water-driven formation of luminescent
1064 Zn_2GeO_4 nanorods from Zn-containing Ge nanoparticles. Cryst Growth Des 8:2264–
1065 2269
1066

1067 Veizer J, Hoefs J (1976) Nature of O^{18}/O^{16} and C^{13}-C^{12} secular trends in sedimentary
1068 carbonate rocks. Geochim Cosmochim Acta 40: 1387−1395
1069
1070 Vivallo W, Broman C (1993) Genesis of the earthy ores at Garpenberg, south central
1071 Sweden. Geol Foren Stockh Förh 115:209–214
1072
1073 Yang P, Lu MK, Song CF, Liu SW, Gu F, Wang SF (2004) Photoluminescence of
1074 Pb^{2+} ions in sol–gel derived Zn_2SiO_4. Inorg Chem Comm 7:268–270
1075
1076 Zheng YF (1993) Calculation of oxygen isotope fractionation in anhydrous silicate
1077 minerals. Geochim Cosmochim Acta 57:1079–1091

Figure 1

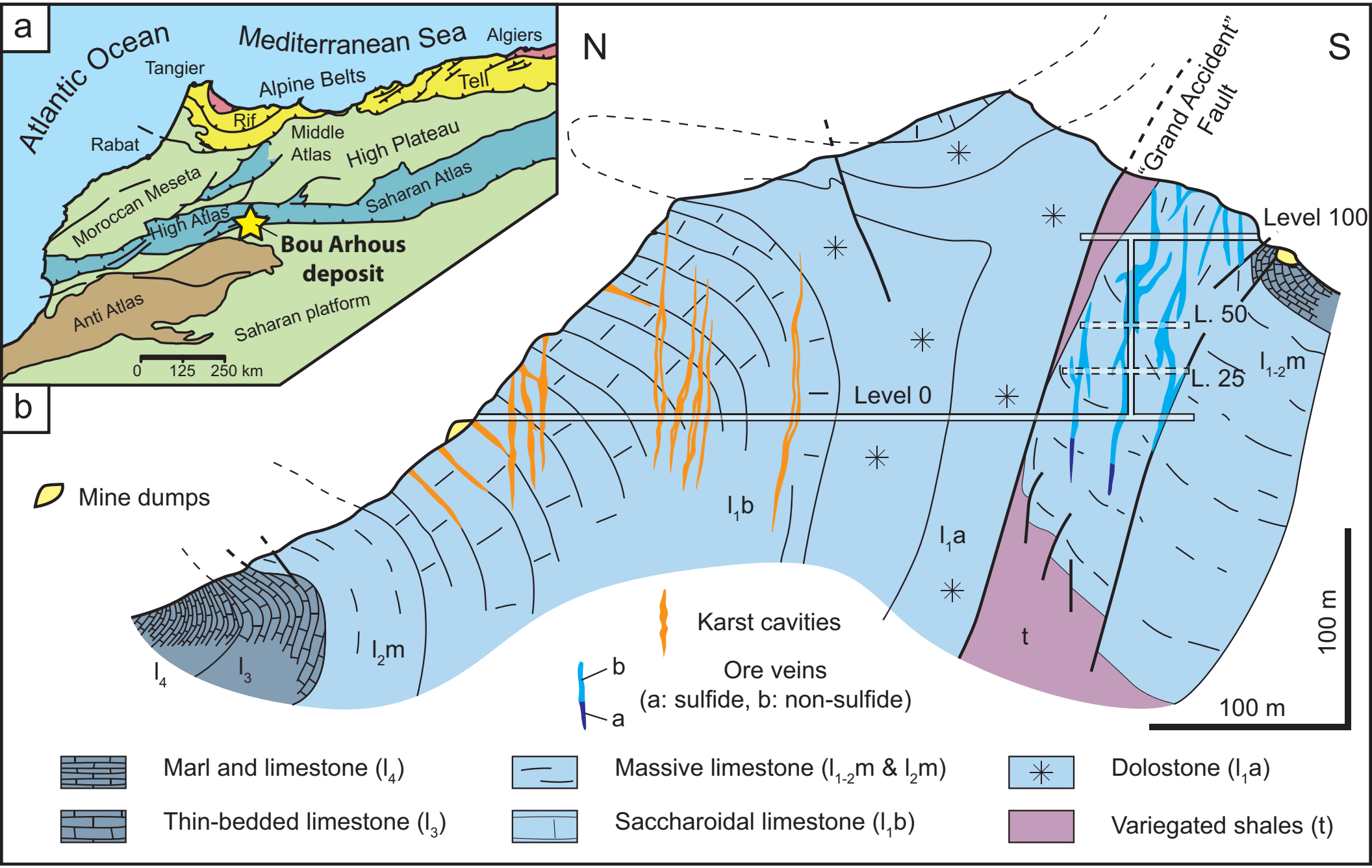
a
Atlantic Ocean
Mediterranean Sea
Algiers
Tangier
Alpine Belts
Tell
Rif
Rabat
Middle Atlas
High Plateau
Moroccan Meseta
Saharan Atlas
High Atlas
Bou Arhous deposit
Anti Atlas
Saharan platform
0 125 250 km
b
N
S
"Grand Accident" Fault
Level 100
L. 50
L. 25
Level 0
l_{1-2}m
l_1b
l_1a
t
l_2m
l_4
l_3
Mine dumps
Karst cavities
b
a
Ore veins
(a: sulfide, b: non-sulfide)
100 m
100 m
Marl and limestone (l_4)
Thin-bedded limestone (l_3)
Massive limestone (l_{1-2}m & l_2m)
Saccharoidal limestone (l_1b)
Dolostone (l_1a)
Variegated shales (t)

Figure 2

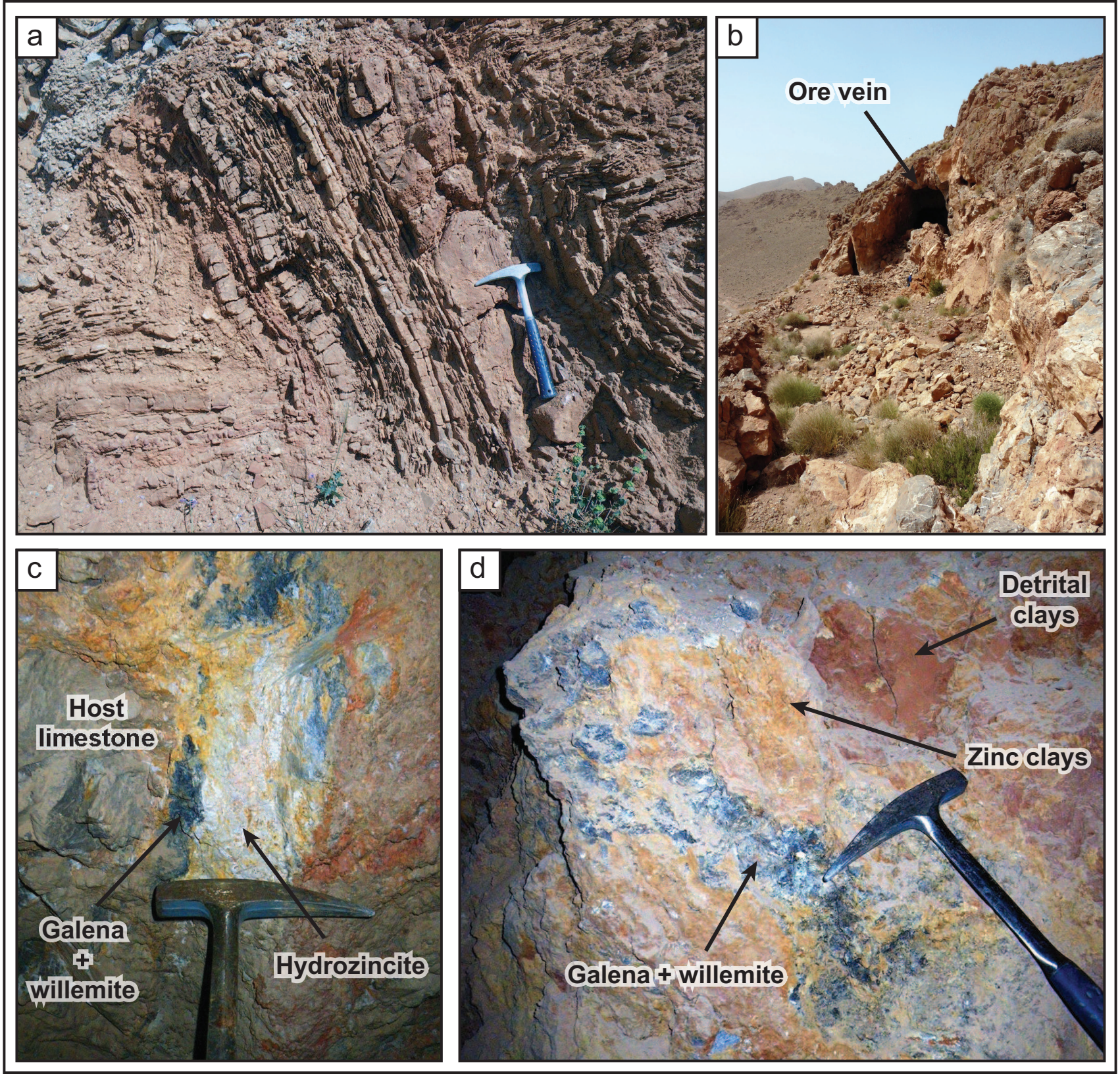
a
b
Ore vein
c
Host limestone
Galena + willemite
Hydrozincite
d
Detrital clays
Zinc clays
Galena + willemite

Figure 3

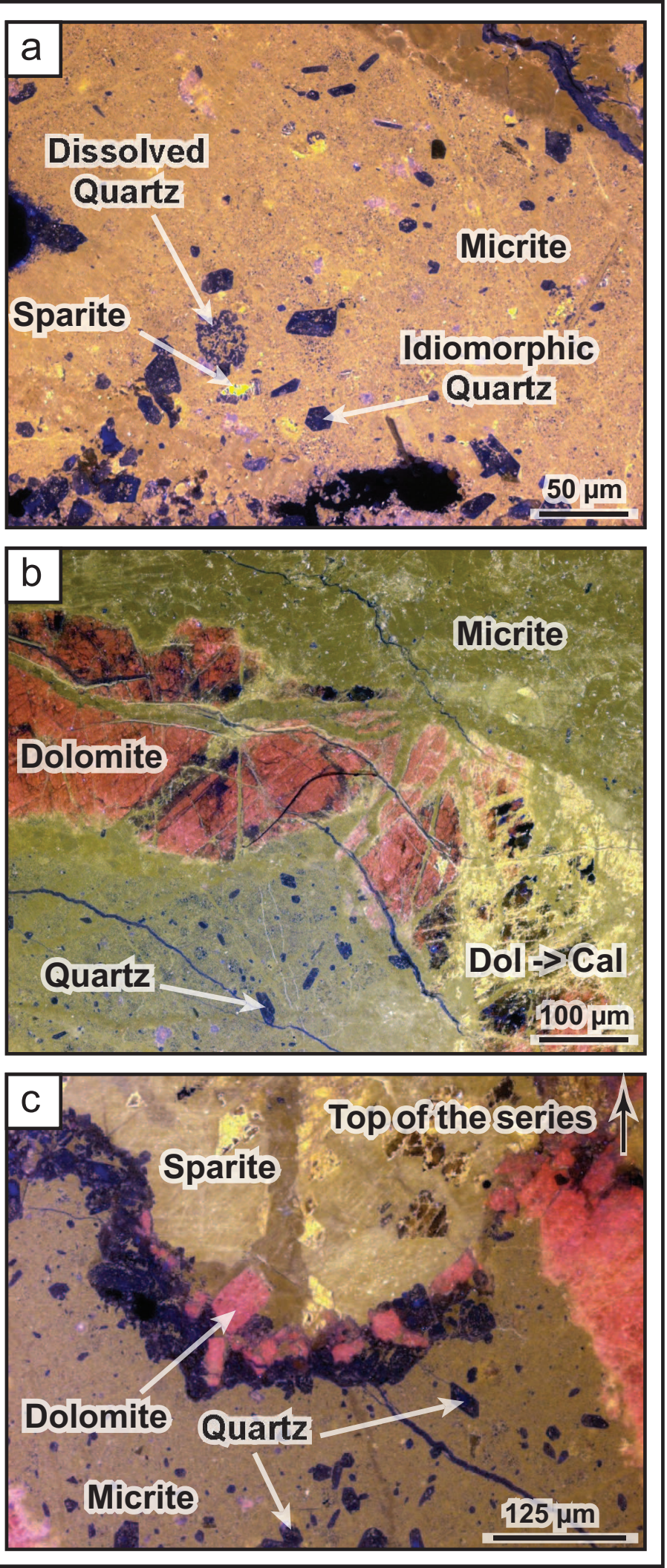
a
Dissolved Quartz
Micrite
Sparite
Idiomorphic Quartz
50 µm
b
Micrite
Dolomite
Dol -> Cal
Quartz
100 µm
c
Top of the series
Sparite
Dolomite
Quartz
Micrite
125 µm

Figure 4

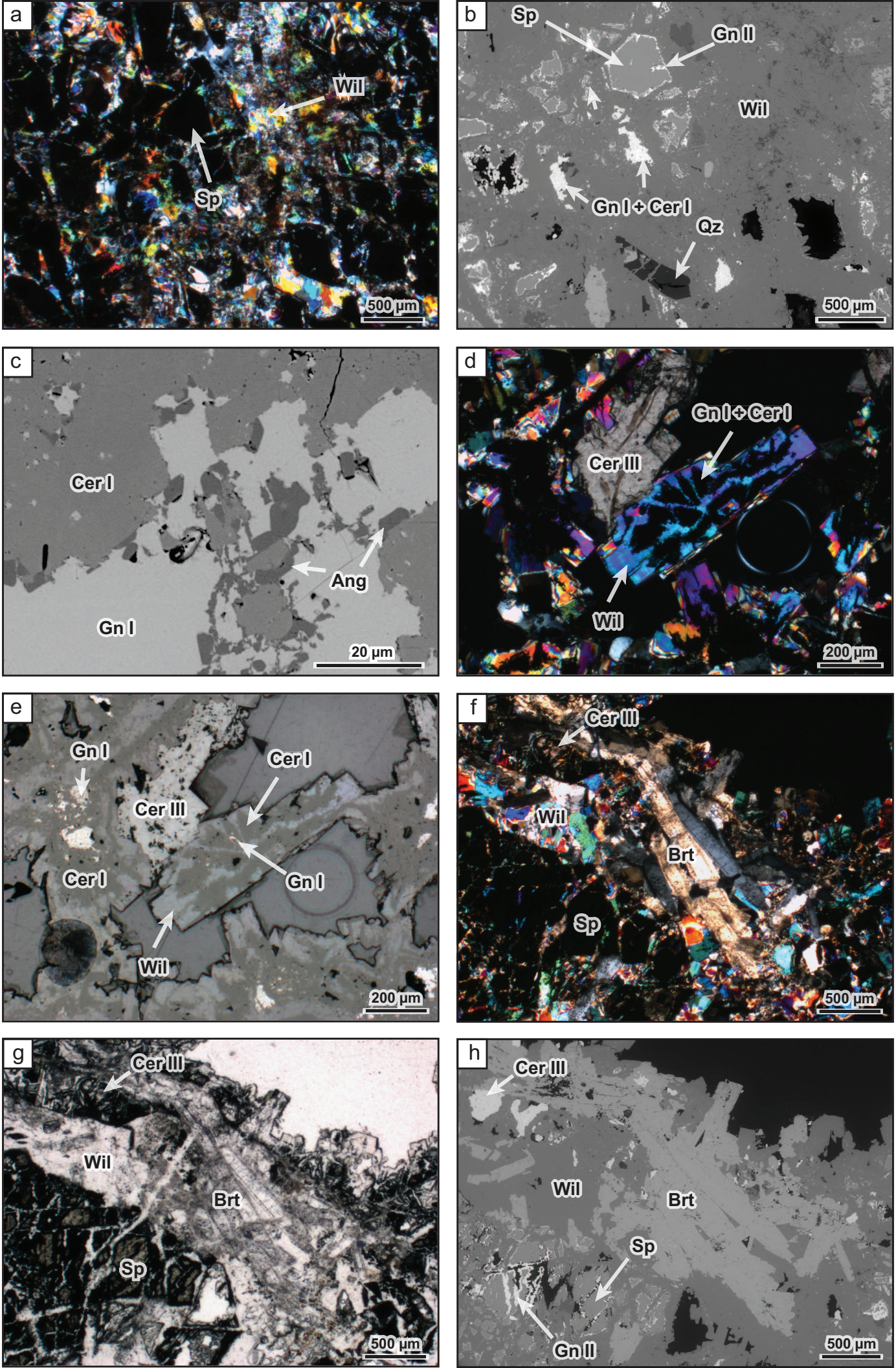
a
Wil
Sp
500 µm
b
Sp
Gn II
Wil
Gn I + Cer I
Qz
500 µm
c
Cer I
Ang
Gn I
20 µm
d
Gn I + Cer I
Cer III
Wil
200 µm
e
Gn I
Cer I
Cer III
Cer I
Gn I
Wil
200 µm
f
Cer III
Wil
Brt
Sp
500 µm
g
Cer III
Wil
Brt
Sp
500 µm
h
Cer III
Wil
Brt
Sp
Gn II
500 µm

Figure 5

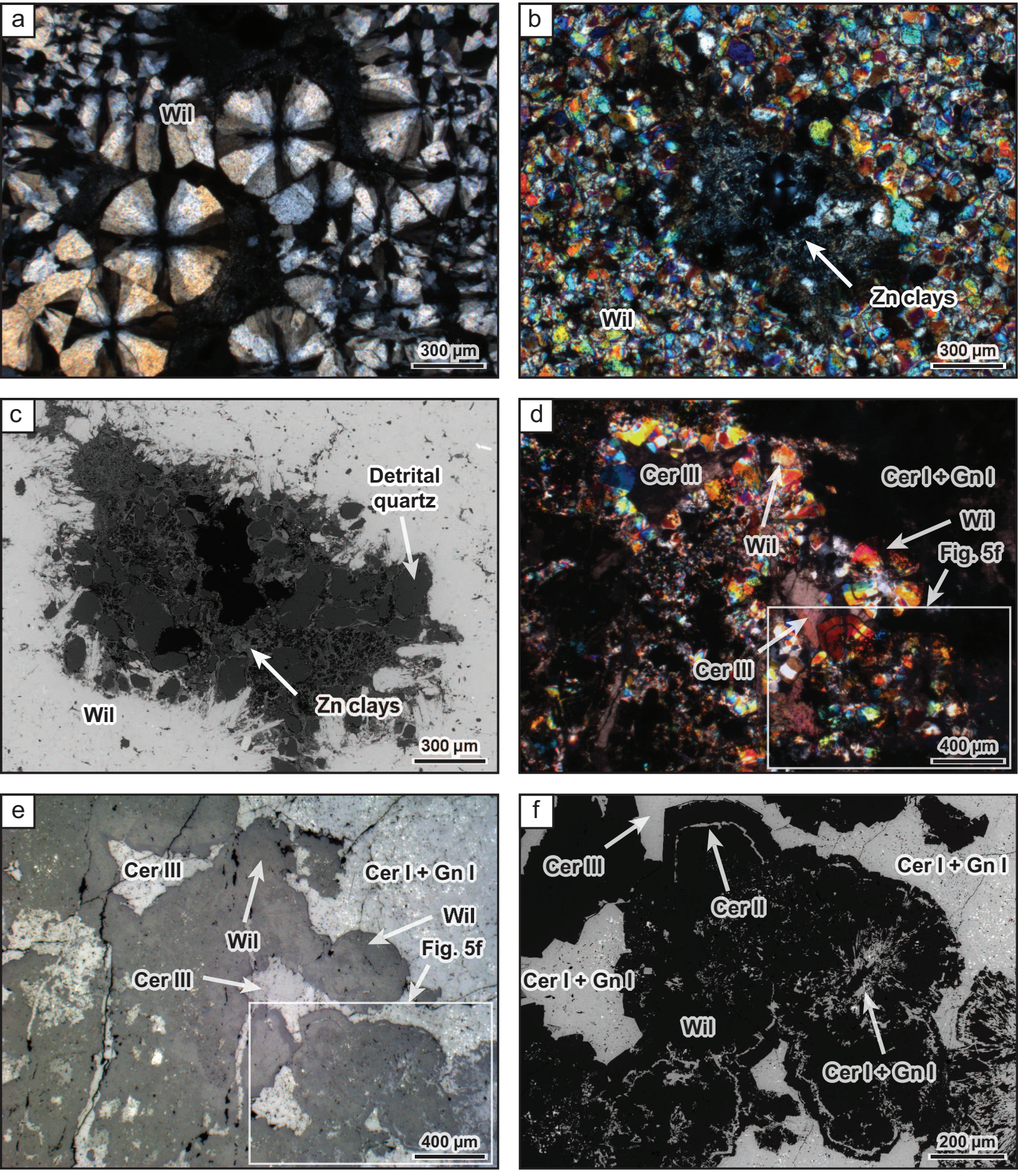
a
Wil
300 µm
b
Zn clays
Wil
300 µm
c
Detrital quartz
Zn clays
Wil
300 µm
d
Cer III
Wil
Cer I + Gn I
Wil
Fig. 5f
Cer III
400 µm
e
Cer III
Wil
Cer I + Gn I
Wil
Fig. 5f
Cer III
400 µm
f
Cer III
Cer II
Cer I + Gn I
Cer I + Gn I
Wil
Cer I + Gn I
200 µm

Figure 6

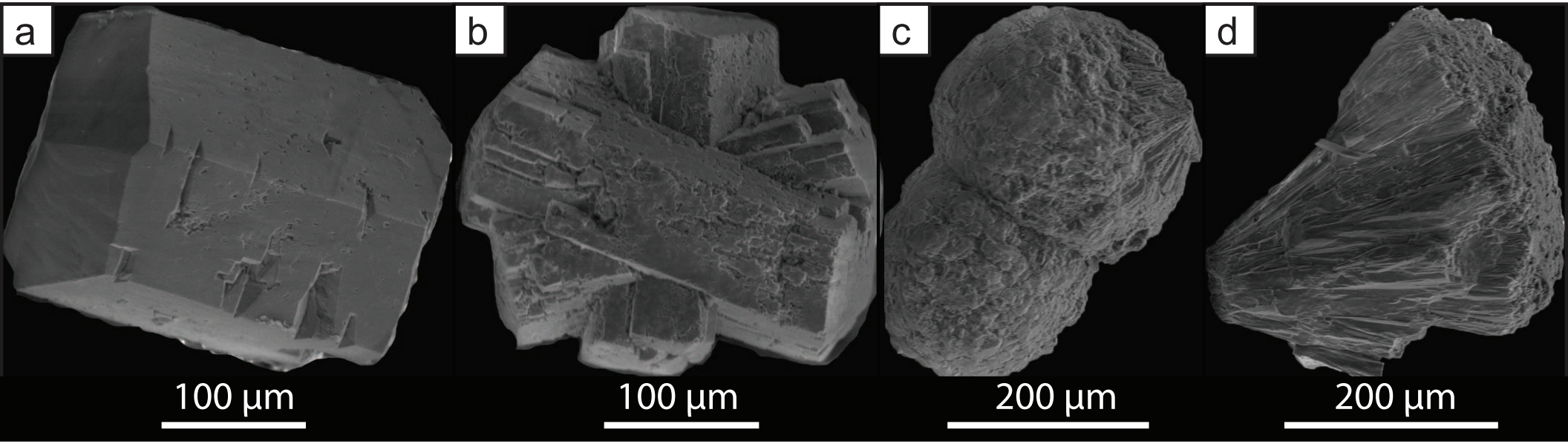

Figure 7

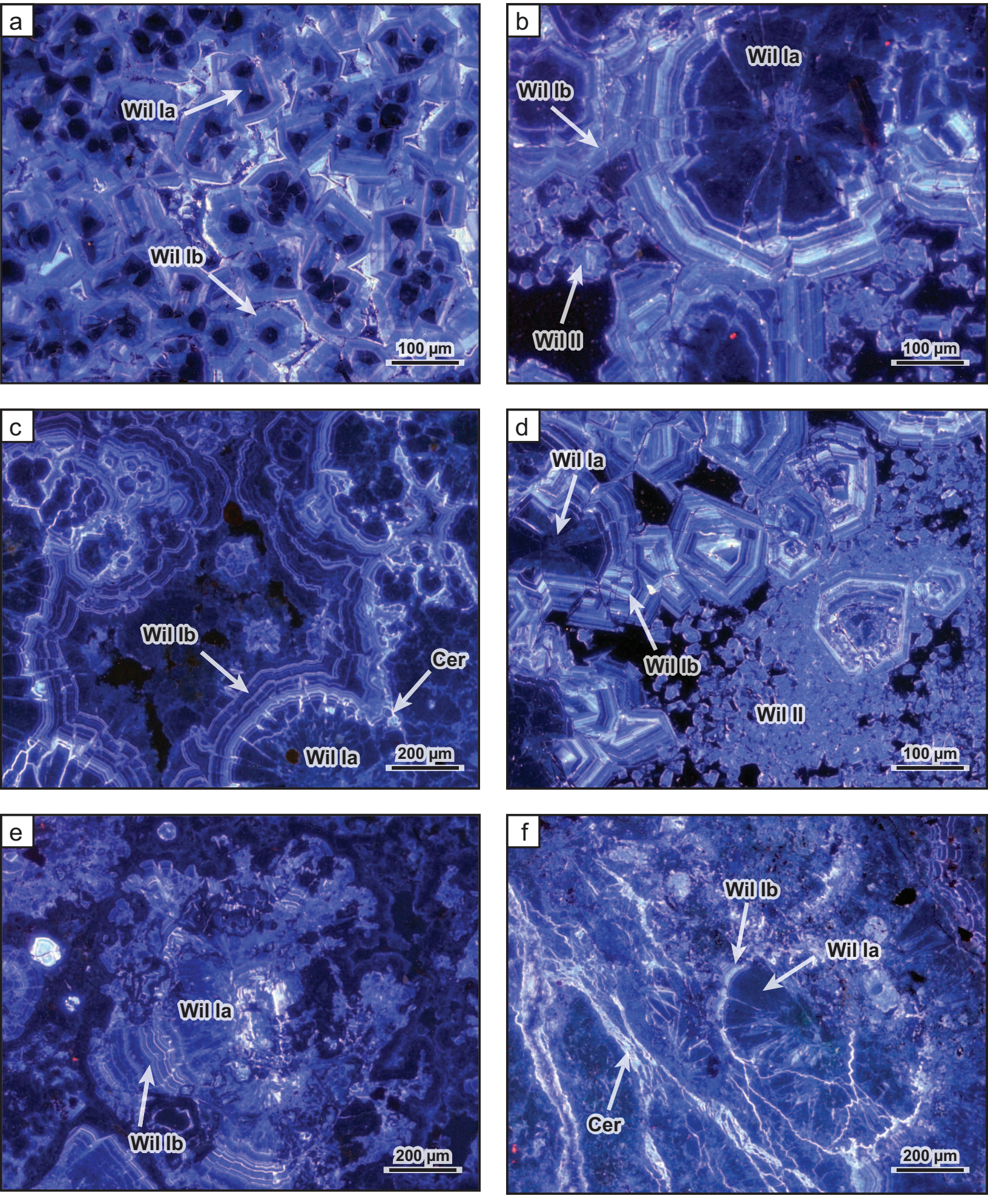
a
Wil Ia
Wil Ib
100 µm
b
Wil Ia
Wil Ib
Wil II
100 µm
c
Wil Ib
Cer
Wil Ia
200 µm
d
Wil Ia
Wil Ib
Wil II
100 µm
e
Wil Ia
Wil Ib
200 µm
f
Wil Ib
Wil Ia
Cer
200 µm

Figure 8

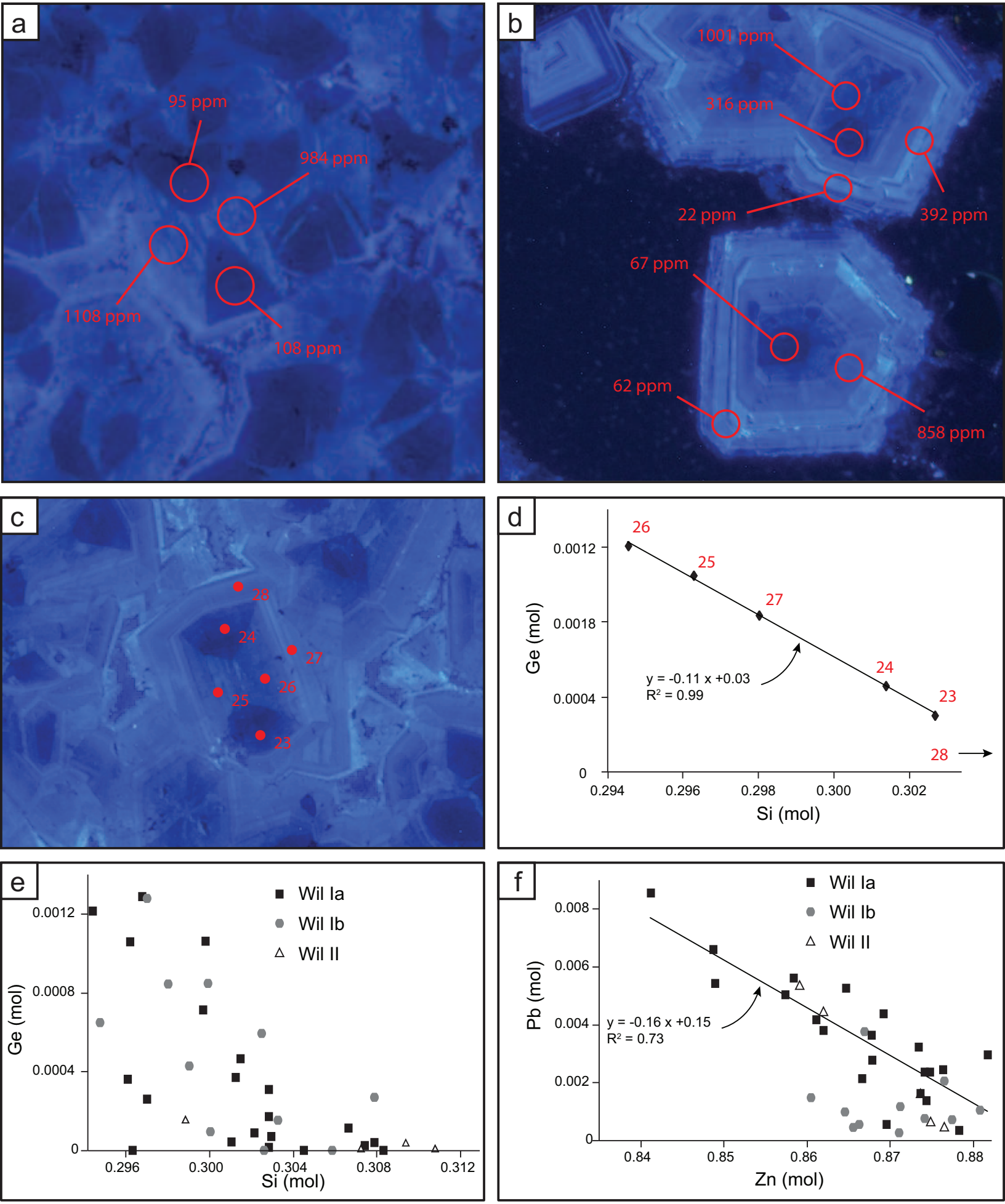
a
95 ppm
984 ppm
1108 ppm
108 ppm
b
1001 ppm
316 ppm
22 ppm
392 ppm
67 ppm
62 ppm
858 ppm
c
28
24
27
26
25
23
d
26
25
27
24
23
28
y = -0.11 x +0.03
R² = 0.99
Ge (mol)
Si (mol)
0.0012
0.0018
0.0004
0
0.294
0.296
0.298
0.300
0.302
e
Wil Ia
Wil Ib
Wil II
Ge (mol)
Si (mol)
0.0012
0.0008
0.0004
0
0.296
0.300
0.304
0.308
0.312
f
Wil Ia
Wil Ib
Wil II
y = -0.16 x +0.15
R² = 0.73
Pb (mol)
Zn (mol)
0.008
0.006
0.004
0.002
0
0.84
0.85
0.86
0.87
0.88

Figure 9

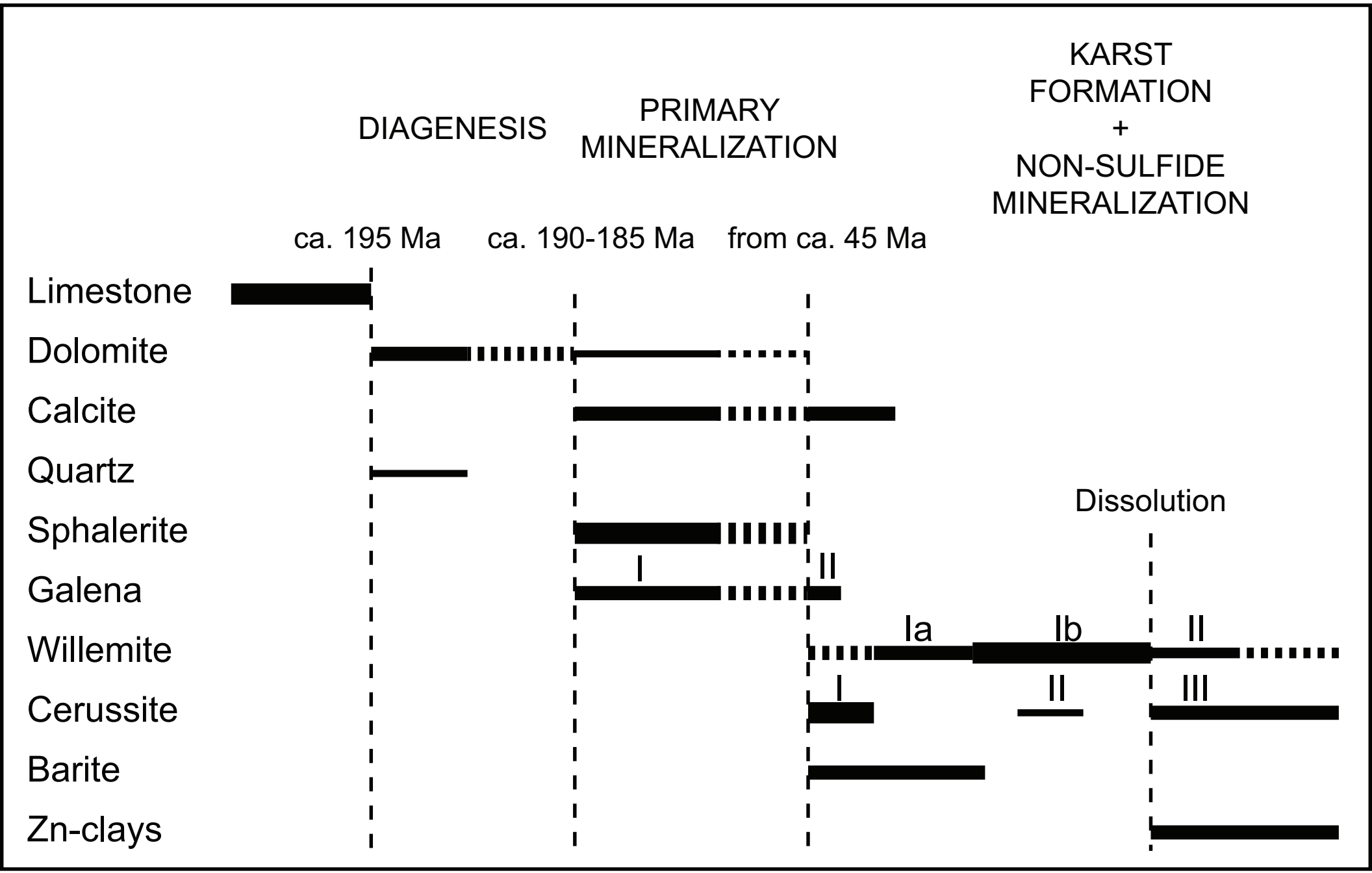
DIAGENESIS
PRIMARY MINERALIZATION
KARST FORMATION + NON-SULFIDE MINERALIZATION
ca. 195 Ma
ca. 190-185 Ma
from ca. 45 Ma
Limestone
Dolomite
Calcite
Quartz
Sphalerite
Galena
Willemite
Cerussite
Barite
Zn-clays
Dissolution
I
II
Ia
Ib
II
I
II
III

Figure 10

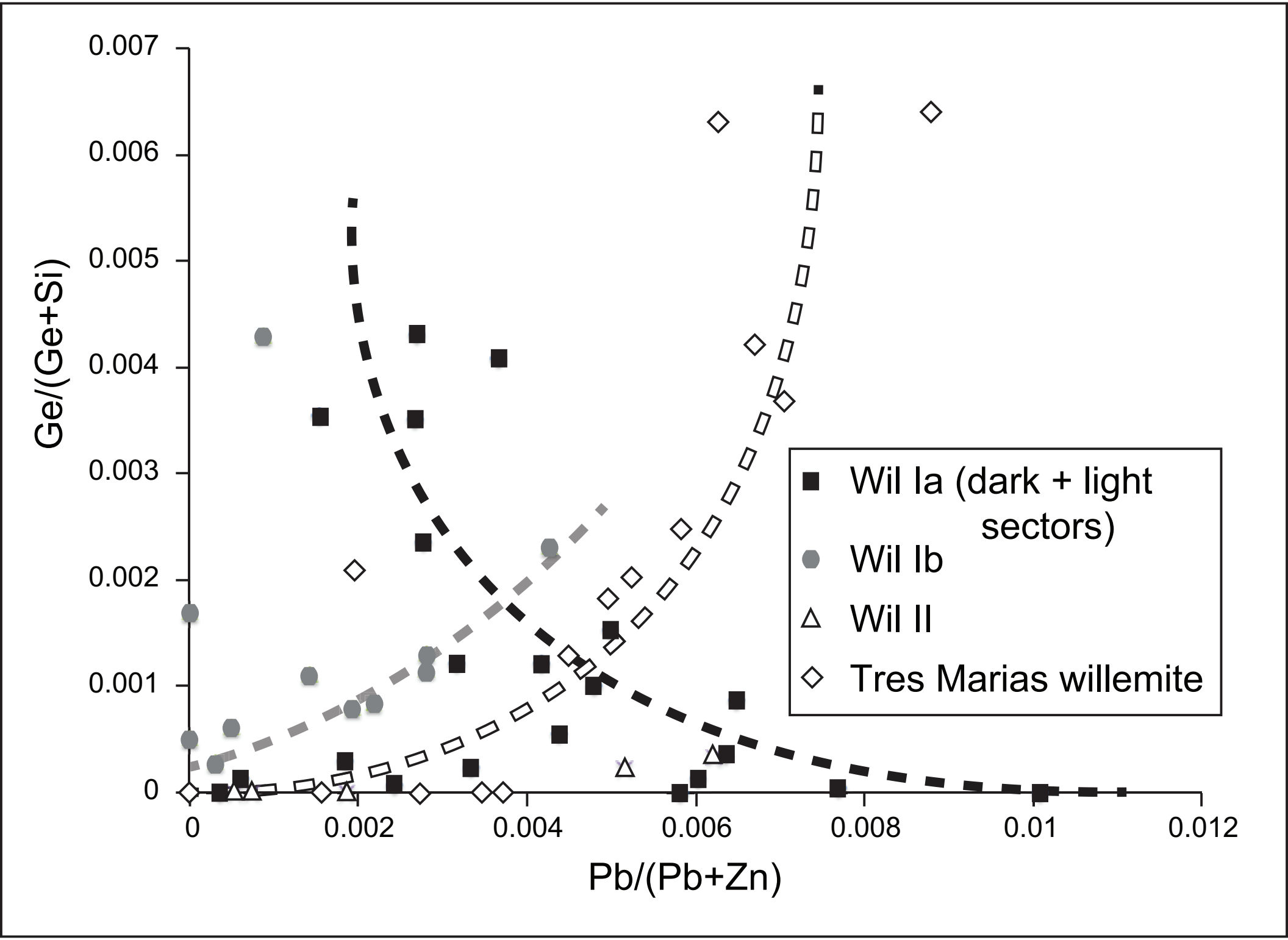
0.007
0.006
0.005
0.004
0.003
0.002
0.001
0
Ge/(Ge+Si)
0
0.002
0.004
0.006
0.008
0.01
0.012
Pb/(Pb+Zn)
Wil Ia (dark + light sectors)
Wil Ib
Wil II
Tres Marias willemite

Figure 11

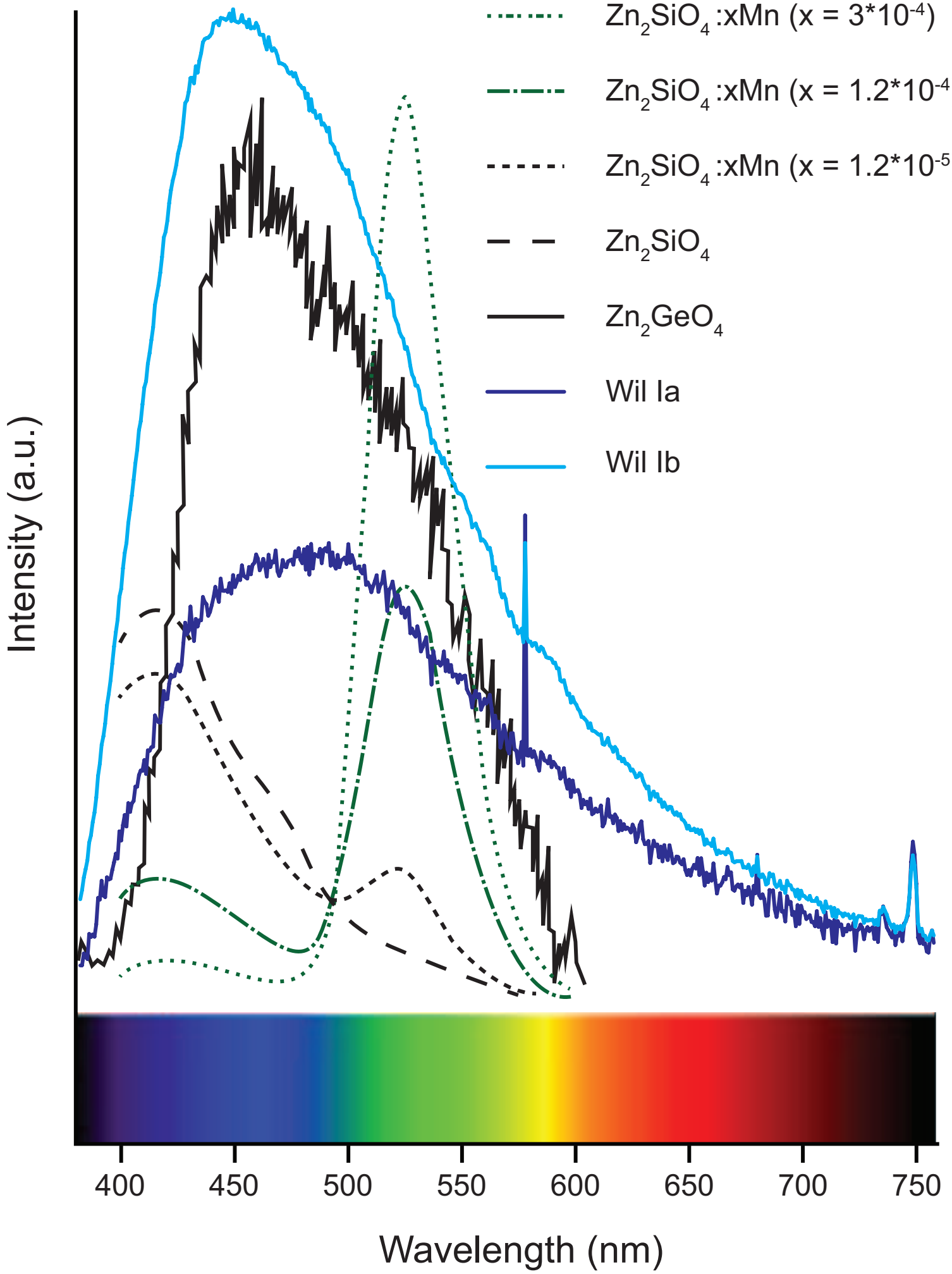
Zn2SiO4 :xMn (x = 3*10-4)
Zn2SiO4 :xMn (x = 1.2*10-4)
Zn2SiO4 :xMn (x = 1.2*10-5)
Zn2SiO4
Zn2GeO4
Wil Ia
Wil Ib
Intensity (a.u.)
400
450
500
550
600
650
700
750
Wavelength (nm)

Figure 12

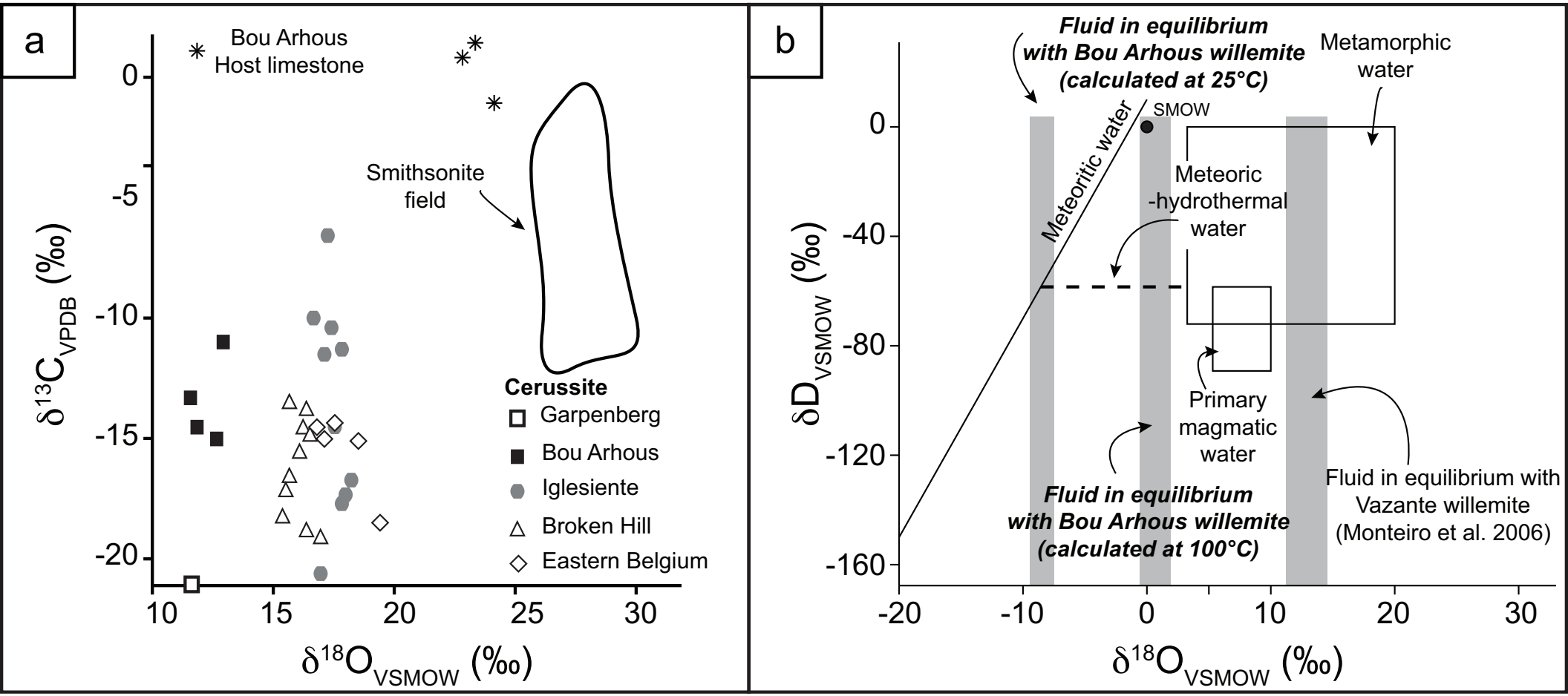
a
Bou Arhous
Host limestone
Smithsonite
field
Cerussite
Garpenberg
Bou Arhous
Iglesiente
Broken Hill
Eastern Belgium
δ13CVPDB (‰)
δ18OVSMOW (‰)
b
Fluid in equilibrium
with Bou Arhous willemite
(calculated at 25°C)
Metamorphic
water
SMOW
Meteoritic water
Meteoric
-hydrothermal
water
Primary
magmatic
water
Fluid in equilibrium
with Bou Arhous willemite
(calculated at 100°C)
Fluid in equilibrium with
Vazante willemite
(Monteiro et al. 2006)
δDVSMOW (‰)
δ18OVSMOW (‰)

Table 1

Sample	BA06A				BA06A			
Type	**Sphalerite n = 7**				**Sphalerite n = 14**			
	Range	**Avg.**	**SD**	**RSD**	**Range**	**Avg.**	**SD**	**RSD**
S	31.91-32.85	32.37	0.34	1	31.33-32.5	32.16	0.29	1
Cd	0.23-0.31	0.27	0.03	10	0.23-0.43	0.29	0.05	17
As	0-0.12	0.04	0.04	105	0-0.12	0.03	0.04	150
Bi	-				-			
Fe	0.04-0.07	0.05	0.01	19	0.04-0.21	0.09	0.04	39
Ag	0-0.06	0.02	0.02	119	0-0.15	0.04	0.05	139
Ni	0-0.02	0.01	0.01	94	0-0.02	0.01	0.01	115
Zn	65.1-66.44	65.85	0.49	1	65.12-66.52	65.878	0.4	1
Pb	-				-			
Ge	-				-			
Cu	0-0.1	0.01	0.01	96	0-0.1	0.01	0.02	175
∑	97.8-99.54	98.63	0.52	0.53	97.08-99.20	98.51	0.59	0.59

BA06A **Galena n = 15**			
Range	**Avg.**	**SD**	**RSD**
12.27-12.58	12.44	0.1	1
0.05-0.12	0.08	0.02	23
0-0.04	0.01	0.01	102
-			
0-0.02	0.01	0.01	142
0-0.29	0.04	0.09	230
0-0.02	0.01	0.01	172
0-0.03	0.01	0.01	142
86.32-87.43	86.91	0.38	1
-			
0-0.03	0.01	0.01	134
98.91-100.02	99.5	0.38	0.38

Table 2

Generation	Wil Ia (dark sectors) n = 15				
	Range	Avg.	SD	RSD	Range
SiO_2	27.29-28.36	27.89	0.31	1	27.12-27.60
GeO_2	0-0.05	0.03	0.01	33	0.04-0.13
Al_2O_3	0-0.07	0.04	0.02	50	0-0.02
ZnO	68.46-71.76	70.26	0.88	1	70.62-71.32
PbO	0.07-1.91	0.88	0.49	56	0.30-0.81
CdO	0-0.01	0.01	< 0.01	-	0-0.01
FeO	0-0.08	0.04	0.02	50	0-0.03
CaO	0-0.05	0.02	0.01	50	0-0.03
MnO	0-0.04	0.04	< 0.01	-	-
Total	97.75-100.31	99.11	0.60	1	98.78-99.54

Generation	Wil Ia (dark sectors) n = 5				
	Range	Avg.	SD	RSD	Range
Ge^{74}	108-316	177	82	46	825-1108

Generation	Wil Ib n = 11				
	Range	Avg.	SD	RSD	Range
SiO_2	27.15-28.32	27.71	0.33	1	27.75-28.69
GeO_2	0-0.13	0.06	0.04	67	0-0.01
Al_2O_3	0-0.06	0.03	0.02	67	0-0.09
ZnO	70.03-71.68	70.84	0.49	1	69.92-71.33
PbO	0.06-0.84	0.26	0.21	81	0.11-1.20
CdO	0-0.01	0.01	<0.01	-	-
FeO	0-0.04	0.03	<0.01	-	0-0.06
CaO	0.01-0.07	0.03	0.01	33	0-0.03
MnO	0-0.07	0.07	<0.01	-	0-0.04
Total	98.26-99.85	98.93	0.51	1	98.90-100.02

Generation	Wil Ib n = 3			
	Range	Avg.	SD	RSD
Ge^{74}	22-858	365	347	95

Wil Ia (light sectors) n = 5		
Avg.	**SD**	**RSD**
27.37	0.17	1
0.10	0.03	30
0.01	0.01	100
71.09	0.22	0
0.57	0.16	28
0.01	<0.01	-
0.03	<0.01	-
0.02	0.01	50
-	-	-
99.16	0.28	0

Wil Ia (light sectors) n = 9		
Avg.	**SD**	**RSD**
941	89	9

Wil II n = 5		
Avg.	**SD**	**RSD**
28.32	0.32	1
0.01	<0.01	-
0.04	0.03	75
70.74	0.58	1
0.56	0.45	80
-	-	-
0.06	<0.01	-
0.02	<0.01	-
0.04	<0.01	-
99.71	0.43	0

Table 3

Bulk cerussite

SAMPLE	$\delta^{13}C$ VPDB	$\delta^{18}O$ VSMOW
BA117	-11.0	12.9
BA118	-13.3	11.6
BA134	-14.5	11.9
BA153	-15.1	12.7

Host carbonates

SAMPLE	$\delta^{13}C$ VPDB	$\delta^{18}O$ VSMOW
BA147	-1.7	23.4
BA158	1.4	24.1
BA159	-1.0	22.9

Bulk willemite

SAMPLE	$\delta^{18}O$ VSMOW	$\delta^{18}O$ VSMOW	$\delta^{18}O$ VSMOW$_f$ [2]
BA117	7.8	-7.4	2.0
BA118	5.9	-9.3	0.1
BA124	5.3	-9.3	-0.5
BA128	5.9	-9.3	0.1
BA130	7.2	8.0	1.4
	7.0	-8.1	1.2
BA131	7.3	-7.8	1.5
BA133	6.9	-8.2	1.1
BA134	7.4	-7.8	1.6
BA135	6.4	-8.8	0.6
BA136*	*12.7*	*-2.5*	*6.9*
	12.5	*-2.7*	*6.7*
BA138	6.2	-9.0	0.4

*: BA136 contains a small proportion of quartz